Advances and Applications in Fluid Mechanics
© 2025 Pushpa Publishing House, Prayagraj, India
https://pphmjopenaccess.com
https://doi.org/10.17654/0973468625008
Volume 32, Number 2, December 2025, Pages 149-196 **P-ISSN: 0973-4686**

BASE PRESSURE CONTROL AND TEMPERATURE DISTRIBUTION ALONG THE DUCT AT SUPERSONIC MACH NUMBER: A COMPREHENSIVE CFD APPROACH-PART II

Amirullah Jais[1], **Ambareen Khan**[2], **Mohammad Nishat Akhtar**[3]
and Sher Afghan Khan[4,*]

[1]Department of Mechanical and Aerospace Engineering
International Islamic University Malaysia
Kuala Lumpur, 53100
Malaysia
e-mail: amirerrol@gmail.com

[2]Centre for Instructional Technology and Multimedia
Universiti Sains Malaysia
11800 USM, Pulau Pinang
Malaysia
e-mail: khanambareen5@gmail.com

Received: July 1, 2025; Accepted: August 1, 2025
2020 Mathematics Subject Classification: 76D10.
Keywords and phrases: base flow, L/D ratio, Mach number, CFD.

*Corresponding author

How to cite this article: Amirullah Jais, Ambareen Khan, Mohammad Nishat Akhtar and Sher Afghan Khan, Base pressure control and temperature distribution along the duct at supersonic Mach number: a comprehensive CFD approach-Part II, Advances and Applications in Fluid Mechanics 32(2) (2025), 149-196. https://doi.org/10.17654/0973468625008

[3]School of Aerospace Engineering
Universiti Sains Malaysia
14300 Nibong Tebal, Penang, Malaysia
e-mail: nishat@usm.my

[4]Department of Mechanical and Aerospace Engineering
Faculty of Engineering
International Islamic University
Kuala Lumpur, 53100, Malaysia
e-mail: sakhan@iium.edu.my

Abstract

The development of space shuttles and high-performance military aircrafts has made the study of turbulent flow in separated regions a key area of research. Researchers are also interested in turbulent flow under transonic and supersonic conditions, particularly when it separates suddenly and expands after the cross-section of the larger duct increases rapidly. Two regions where the shear layer forms are the separated flow and the main flow. The split streamline reattaching to the duct causes significant drag and creates a recirculation zone where the pressure is lower than in the surrounding air. This study investigates the use of quarter-circular ribs to regulate base pressure as a passive control method, where the shear layer hits the straight part of the rib and the curved part is downstream. Computational simulations investigate how the rib radius and placement near a backward-facing step influence flow behavior, including recirculation and vortex formation. In the study, the inertia parameters considered were a Mach number of $M = 1.7$ and the nozzle pressure ratio (NPR) in the range of 3 to 11. The geometrical parameters considered were the area ratio $(A_2/A_1 = 4)$, the cross-sectional area of the duct-to-nozzle exit, and the length-to-diameter (L/D) ratio, ranging from 1 to 6. The quarter-circle radius considered was 1.5 mm, 2 mm, and 3 mm, and the ribs were located at $L/D = 0.5,\ 1,\ 1.5,$ and 2. The goal is to identify the optimal rib geometry and location that maximizes aerodynamic efficiency. The results show that the optimum rib radius and locations are 3 mm and $L/D = 2$. The rib radius of 1.5 mm does not show any definite pattern. In contrast, the 3 mm rib radius exhibits a progressive increase in the base at various locations within the duct. Hence, a 3 mm rib radius seems to be the best option if the application is to reduce the base drag to a considerable level.

1. Introduction

Research on turbulent base flows is ongoing due to their significant impact on the operation and durability of aerodynamic vehicles. Base flows are represented by a massive shear layer partition that forms at the base due to an abrupt change in the rear geometry. Two highly undesired problems are caused by the divided flow in the base region: an increase in drag and instability of the base. The instability causes pummeling phenomena and unpredictable loads; the drag force, known as base drag force, can account for up to 60% of the total drag in some situations. Mach number, the type of boundary layer before separation, and geometry are some of the crucial characteristics that affect base flows.

A wide range of flow regimes, from subsonic to hypersonic speeds, have been studied to comprehend the base fluxes. Even with these efforts, accurate insight is still elusive. It is clear from earlier research that the growth and reattachment of the shear layer, the recirculation zone near the base, the shedding of the vortex, and the interfaces between them are the primary determinants of the flow dynamics in the base area. The literature reports on research involving various base flow parameters.

Two groups of study results can be distinguished: one focusing on the flow field behavior near the base and the other on methods to regulate the base pressure and reduce the base drag. Determining the fundamental characteristics, instruments, and behavior of base flow is essential to these investigations. The following are a few previous evaluations. The pressure at the base may be similar to that in a significant recirculation region of the backward-facing step, according to a study conducted by the researchers. Researchers contend that large-scale coherent motions at a Strouhal number specified as $St = f(D/U)$ of 0.2 dominate an ordered structure based on their computational investigation of an axisymmetric turbulent boundary layer and reattaching flow.

Due to the issue above, numerous researchers attempted to limit the base pressure; however, we were unable to regulate the skin friction drag due to mission restrictions. At a point in the expanded duct, the nozzle flow separates during exit and reattaches. Reattachment length is the distance between the nozzle exit and the reattachment point. The nozzle pressure ratio, Mach number, and area ratio all significantly impact this location on the expanded duct wall. Therefore, this publication examines some of the most recent strategies for optimizing base pressure and drag using passive control techniques. Controlling this low pressure in the base region and bringing it close to atmospheric pressure is urgently needed to achieve nearly negligible base drag. The base drag can be reduced by increasing the base pressure and weakening the strong vortex in the recirculation zone.

Active and passive controls are the two methods used to control the base pressure. Blowing or suction techniques are used to achieve dynamic control of base fluxes, which necessitates an outside energy source. Its ability to be turned on and off as needed is the primary benefit of this kind of control. The primary drawback of this type of control is the reliance on a high-energy source, which is not readily available, and the additional weight it imposes on aeronautical vehicles, such as rockets and launch vehicles, where weight is a critical factor. Obtaining a second external energy source is not always possible.

On the other hand, with passive control, the base pressure is managed by utilizing the geometrical variations of the structures, which include splitter plates, boattail, ribs, cavities, and locked vortex devices. In contrast to active control, passive control does not need an external energy source, which makes it simple to build, less expensive, and less complicated to design. Figure 1 illustrates the intricate flow field of abrupt expansion. The separation of the boundary layer, the establishment of the principal recirculation zone at the base corner, and the reattachment at the wall are all visible. By disrupting this flow field, the passive control raises the base pressure and lowers the base drag.

This study employs a regulation of base pressure through passive control using quarter-circular ribs for an area ratio of 4 at a supersonic Mach number of Mach 1.7. By altering the flow field near the base, quarter ribs can effectively manipulate base pressure. Optimizing the geometry of these passive control devices is crucial, as any increase in base pressure and consequent decrease in base drag will significantly affect the aerodynamic efficiency.

2. Literature Review

Suddenly, expanded flows at sonic and supersonic Mach numbers present complex challenges due to flow separation, recirculation zones, and base pressure deficits, which contribute significantly to aerodynamic drag. Researchers have extensively explored passive control methods, such as incorporating ribs, cavities, and other geometric modifications, to mitigate these issues and enhance base pressure recovery. Khan et al. [1] conducted experimental investigations on the use of semi-circular ribs in suddenly expanded flows at both sonic and supersonic Mach numbers. Their study compared experimental results with predictions from single-layer and deep neural network models, demonstrating that the inclusion of ribs effectively increased base pressure and reduced flow separation.

In a complementary study, Khan et al. [2] examined the effect of ribs as passive control devices on base pressure at sonic Mach numbers. Their findings indicated that the presence of ribs led to a significant increase in base pressure, attributed to the disruption of the recirculation zone and the promotion of earlier flow reattachment. Further exploring rib geometries, Khan et al. [3] analyzed the impact of various rib configurations in a suddenly expanded flow at sonic Mach numbers. The study revealed that specific rib shapes and placements could optimize base pressure recovery, highlighting the importance of geometric considerations in passive control strategies. Numerical simulations have also played a pivotal role in understanding flow behaviors. Khan et al. [4] performed simulations of suddenly expanded flows from converging nozzles at sonic Mach numbers, providing insights into velocity distributions and base pressure variations. Their work highlighted the importance of nozzle geometry and expansion ratios in shaping flow characteristics.

Advancements in computational fluid dynamics (CFD) have facilitated more comprehensive analyses. Khan et al. [5] conducted a CFD study on base pressure control using quarter ribs in sudden expansion ducts at sonic Mach numbers. The research demonstrated that quarter ribs could effectively manipulate the flow field, leading to enhanced base pressure and reduced drag. Building upon this, Khan et al. [6] explored the use of semi-circular ribs at critical Mach numbers. Their findings emphasized the effectiveness of these ribs in controlling base pressure, particularly at specific Mach number regimes.

Nurhanis et al. [7] investigated base pressure control at supersonic Mach numbers in suddenly expanded flows, emphasizing the role of passive devices in managing shock-boundary layer interactions. Their findings indicated that appropriately designed control elements could mitigate adverse pressure gradients and stabilize the flow. Fakhruddin et al. [8] analyzed base pressure control with ribs at Mach 1.2 using CFD methods. The study highlighted the effectiveness of rib placements in altering flow structures and improving pressure distributions, reinforcing the utility of passive controls in supersonic applications.

Khan et al. [9] examined velocity distribution and base pressure analysis of under-expanded nozzle flow at Mach 1.0. Their research provided valuable data on flow characteristics in such conditions, aiding in the design of effective control strategies. Incorporating machine learning, Khan et al. [10] assessed the performance of supervised learning algorithms in classifying flow behaviors. Their work suggested that machine learning techniques can complement traditional computational fluid dynamics (CFD) methods in designing efficient flow control mechanisms. Mishra et al. [11] focused on determining shock standoff distances for wedges in supersonic flow, contributing to the understanding of shock-wave interactions in high-speed flows.

Chaudhary et al. [12] explored base pressure control using quarter-circle ribs in suddenly expanded ducts at screech-prone Mach numbers $(M = 1.8)$. Their study demonstrated the potential of such ribs in mitigating screech phenomena and enhancing flow stability. Mahaboobali et al. [13] investigated the passive control of base flows, analyzing the impact of quarter-rib radius and locations at sonic Mach numbers. Their findings emphasized the importance of rib geometry and placement, as they are not effective for flow control. Further, Chaudhary et al. [14] studied the control of suddenly expanded flow using quarter ribs for an area ratio of 4.84 at Mach 2. Their research highlighted the significance of area ratios in designing effective passive control mechanisms. Khan et al. [15] conducted an extensive CFD study on supersonic flow control with quarter ribs in ducts. Their work provided comprehensive insights into the effectiveness of quarter ribs across various flow conditions. Shetty et al. [16] performed a comprehensive CFD analysis on base pressure control using quarter ribs at Mach 1.3. Their study reinforced the utility of quarter ribs in managing base pressure across different Mach numbers. Bellary et al. [17] conducted numerical simulations of base pressure and its control in suddenly expanded ducts at Mach 1.6 using quarter-circular ribs. Their findings contributed to the optimization of rib designs for effective flow control.

In another study, Bellary et al. [18] analyzed the computational aspects of thrust generated by converging-diverging nozzles at different diverging angles. Their research provided valuable data for optimizing nozzle designs in high-speed applications. Anuar et al. [19] investigated the effect of cavity geometry and location on base pressure in suddenly expanded flows at Mach 2.0 for an area ratio of 3.24. Their study emphasized the role of cavity design in passive flow control strategies. Bashir et al. [20] conducted a numerical investigation of turbulence models with an emphasis on turbulent intensity at low Reynolds number flows. Their work contributed to the selection of appropriate turbulence models for accurate flow simulations.

Baig et al. [21] explored the control of base flows with micro-jets, demonstrating the effectiveness of active control methods in managing base pressure and reducing drag. Rehman and Khan [22] focused on controlling base pressure with micro-jets, providing insights into the design and implementation of active flow control techniques.

Faheem et al. [23] conducted an experimental study on the mean flow characteristics of a supersonic multiple jet configuration, contributing to the understanding of complex jet interactions in high-speed flows. Sajali et al. [24] performed a numerical investigation of the flow field of a non-circular cylinder, providing data relevant to flow control around bluff bodies. Khan et al. [25] investigated the passive flow control management of base drag in compressible subsonic flow using multiple cavities, emphasizing the effectiveness of cavity configurations in reducing drag.

In another study, Khan et al. [26] conducted a computational fluid dynamics (CFD) analysis of a human-powered submarine to minimize drag, applying flow control principles to underwater vehicles. Khan et al. [27] investigated the passive control of base drag employing dimples in subsonic suddenly expanded flow, demonstrating the potential of surface modifications in drag reduction. Aabid et al. [28] optimized the dry sliding wear behavior of aluminum-based hybrid metal matrix composites using experimental and design of experiments (DOE) methods, contributing to material selection in flow control applications.

The findings of this study will be convenient in the design and development of aerospace vehicles. The database obtained through this study can be used to find the optimum dimensions of the rockets and missiles. Any increase in the base pressure, and hence a decrease in the total base drag, will be beneficial in arriving at the optimum design of aerospace launch vehicles.

3. Methodology: Finite Volume Method

3.1. Governing equations

The following hypotheses are taken into consideration:

(i) Turbulent flow is considered because of the turbulent viscous dissipation effects.

(ii) The fluid's viscosity varies with temperature and is compressible.

(iii) At atmospheric pressure, the flow exits the duct.

(iv) Shetty et al. [16] employed the standard *k*-ε turbulence model to simulate the internal flow. As a result, the standard *k*-ε turbulence model is applied to the circumstance. Sutherland's three-coefficient viscosity model is expressed as follows:

$$\mu' = \mu'_o \left(\frac{T_a}{T_{a,o}} \right)^{3/2} \frac{T_{a,o} + S'}{T_a + S'}. \tag{1}$$

The reference viscosity value in kg/m-s is denoted as μ'_o, where μ' represents the viscosity. T_a denotes static temperature, and S' is the temperature-dependent Sutherland constant.

Continuity equation for unsteady compressible flow

The equation for mass balance is as follows:

$$\frac{\partial \rho}{\partial t} + \underline{\nabla} \cdot (\rho \underline{V}) = 0, \tag{2}$$

where the fluid's velocity is denoted by V.

The equation for momentum balance is:

$$\frac{\partial}{\partial t}(\rho \underline{V}) + \underline{\nabla} \cdot (\rho \underline{VV}) + \underline{\nabla} p = \underline{\nabla} \cdot [2\mu(\underline{\nabla V})_o^s] + \underline{\nabla} \cdot (\tau_{=Re}), \tag{3}$$

where $(\underline{\nabla V})_o^s = (\underline{\nabla V})^s - \frac{1}{3}(\underline{\nabla} \cdot \underline{V})\underline{I}$, $(\underline{\nabla V})^s = \frac{\underline{\nabla V} + \underline{\nabla V}^T}{2}$, and $\tau_{=Re}$ is the turbulent stress tensor.

The formulae for total energy are as follows:

$$\frac{\partial}{\partial t}\left[\rho\left(\frac{1}{2}V^2 + u_{\text{int}}\right)\right] + \underline{\nabla}\left[\rho\left(\frac{1}{2}V^2 + u_{\text{int}}\right)\underline{V}\right]$$

$$= \underline{\nabla}(\lambda\underline{\nabla}T - p\underline{V} + 2\mu\underline{V} \cdot (\underline{\nabla V})_o^s + \underline{V} \cdot \tau_{=Re}), \tag{4}$$

where u_{int} is the internal energy, and λ is the thermal conductivity.

Many internal flow simulations use the *k*-ε turbulence model due to its affordability, resilience, and sufficient accuracy. The Ansys Fluent program incorporates the *k*-ε turbulence model used in this research. The *K*-equation allowed us to calculate the turbulent kinetic energy:

$$\frac{\partial}{\partial t}(\rho k) + \underline{\nabla} \cdot (\rho\underline{V}k) = \underline{\nabla} \cdot \left[\left(\mu + \frac{\mu_t}{\sigma_k}\right)(\underline{\nabla}k)\right] - \rho\varepsilon + M_x. \tag{5}$$

The turbulent kinetic energy dissipation rate is denoted by ε, the turbulent Prandtl number is $\sigma\text{-}k$, and M_x is the turbulence generation. Precisely, the dissipation is controlled by

$$\frac{\partial(\rho\varepsilon)}{\partial t} = -\underline{\nabla} \cdot (\rho\varepsilon\vec{V}) + \underline{\nabla} \cdot \left[\left(\mu + \frac{\mu_T}{\sigma_\varepsilon}\right)\nabla\varepsilon\right] - C_1 f_1\left(\frac{\varepsilon}{k}\right)M - C_2 f_2 \frac{\varepsilon^2}{k}, \tag{6}$$

where $\mu_t = \rho f_\mu C_\mu k^2/\varepsilon$ denotes turbulent viscosity, and the arbitrary constants are denoted as $\overline{C_\mu} = 0.09$, $\overline{C_1} = 1.44$, $\overline{C_2} = 1.92$, $\overline{f_\mu} = 1$, $\sigma_k = 1.0$, and $\sigma_\varepsilon = 1.3$.

3.2. Geometry and modelling

The simulation procedure employed a finite volume method (FVM), specifically using Workbench 2024/R2 software to analyze the fluid flow in the nozzle. The model was designed as shown in Figure 1, with geometries listed in Table 1, and generated using a Design Modeler for two orientations, as depicted in Figures 1(a) and (b), with specified boundary conditions.

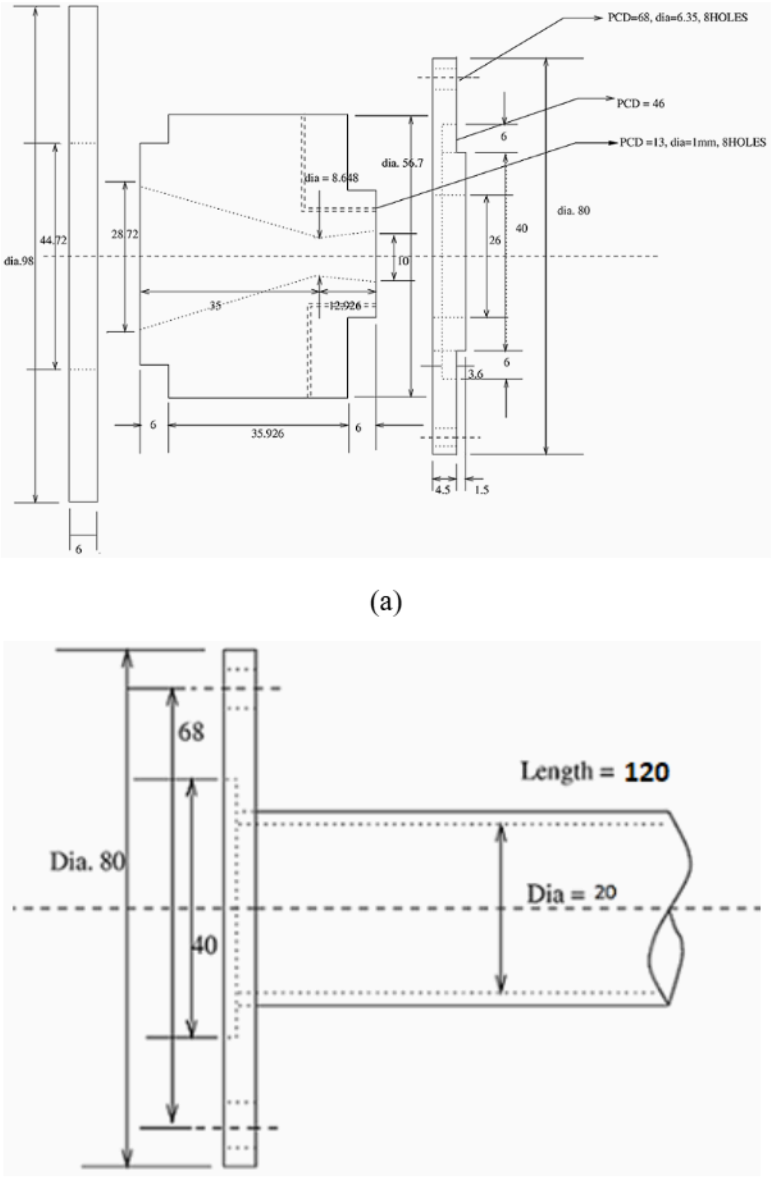

(a)

(b)

Figure 1. Nozzle and duct dimensions.

Table 1. Geometries of design model

Parameters	Dimensions
Nozzle inlet diameter	28.72 mm
Nozzle outlet diameter	10 mm
Nozzle throat diameter	8.468 mm
Converging nozzle length	35 mm
Diverging nozzle length	12.926 mm
duct diameter	20 mm
Duct length	Varies from 1D to 6D
Rib radius	1 mm, 1.5 mm, 2 mm, 2.5 mm, 3 mm
Rib locations	0.5D, 1D, 1.5D, 2D, 3D

Figure 2. Rib orientations.

3.3. Meshing and boundary conditions

A high-quality mesh, characterized by good aspect ratios, smooth transitions between cells, and the absence of skewed or distorted elements, is crucial for accurate and efficient simulations. By choosing the free-face mesh type, the 2D model is of the structured mesh type in this case. CFD meshing involves dividing the computational domain into discrete cells or elements. A high-quality mesh, characterized by good aspect ratios, smooth transitions between cells, and the absence of skewed or distorted elements, is crucial for accurate and efficient simulations. Appropriate and refined face meshing, as shown in Figure 3, was employed, where a grid size was carefully determined to ensure convergence and reliable results. The mesh density should be sufficient to capture relevant flow features, such as boundary layers, shock waves, and vortices, without leading to excessive computational cost. A mesh independence study was conducted to validate the mesh quality and ensure grid independence. The 2D model was employed with a rectangular structured mesh where elements were sized based on the edge lengths due to the selection of the free-face mesh.

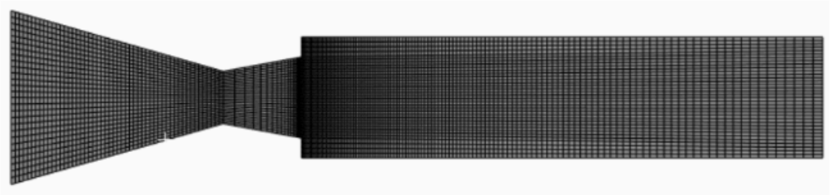

(a) Without rib

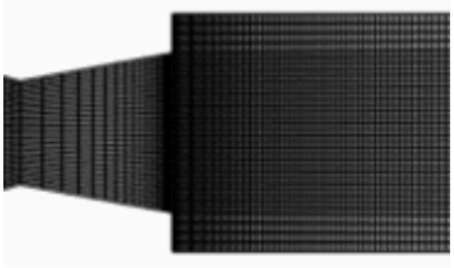

(b) Mesh closed up without rib

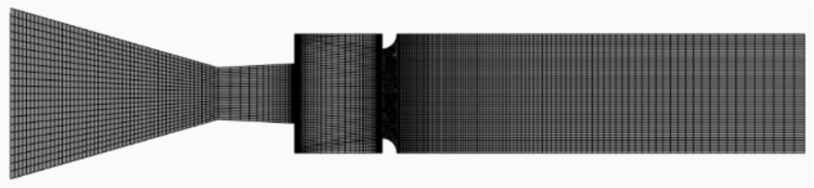

(c) With rib for orientation 2

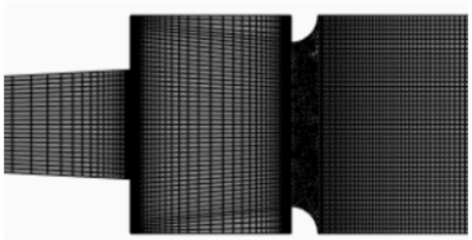

(d) Mesh closed up on with rib for orientation 2

Figure 3. Mesh model for mesh independence study.

Table 2. Boundary conditions of the design model

Zone	Geometry
Inlet	Nozzle inlet
Wall	Convergent-divergent nozzle wall
Base wall	Duct inlet
Axis	*x*-axis (axisymmetric line)
Rib	Rib wall
Outlet	Duct outlet

3.4. Assumptions and fluid properties

Assumptions are used to replicate the flow activities in the precise physical environment. Appropriate mathematical and numerical models are selected to make the governing equations.

To solve the governing equations simultaneously, numerical modeling requires selecting the appropriate mathematical models, including the governing equations, boundary conditions, mesh quality, and numerical method. Despite its limitations in accurately representing physical phenomena, the computational method has been trusted for decades and offers sufficient insight into flow behavior. As a result, this calls for careful consideration of elements that closely resemble the flow behavior. This study pinpoints the presumptions that jeopardize the precise physical state. The following are the presumptions and characteristics covered in this study:

(i) The flow is assumed to be a steady 2D flow because the geometry is symmetric.

(ii) The density of the air is variable.

(iii) Since turbulent flow has a significant impact on turbulent viscous dissipation at a given flow velocity, it is taken into consideration.

(iv) The viscosity of the fluid is dependent on the temperature.

(v) At the standard atmospheric pressure, the flows leave the duct. At normal ambient pressure, the flows leave the duct.

Since the flow via the nozzle is considered turbulent, the compressible flow field is represented by the k-ε standard model. The subsequent equations most appropriately characterize the turbulent flow.

3.5. Numerical and experimental results validation

The study initially involved replicating the experiment conducted by Rathakrishnan, in which five equidistant ribs were placed within a duct, as shown in Figure 4 (Rathakrishnan [29]), for method validation purposes. It also serves as a source of understanding the physics of the flow inside the duct. Rathakrishnan's findings on the variation in base pressure with different NPR and L/D ratios, as shown in Table 3, served as a benchmark for comparison. Both controlled (with ribs) and uncontrolled (without ribs) flow configurations were simulated to ensure the accuracy of the numerical results.

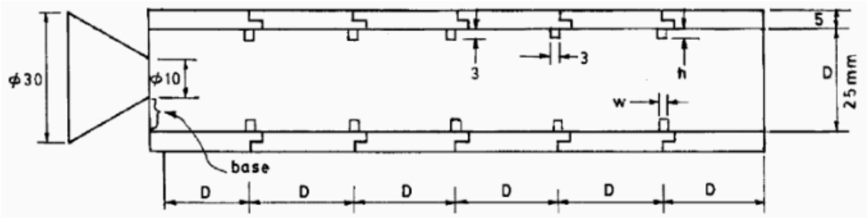

Figure 4. 2D simulation model of the Rathakrishnan's experimental study (Rathakrishnan [29]).

Table 3. Geometries of the validation model

Parameters	Dimensions
Nozzle inlet diameter	30 mm
Nozzle outlet diameter	10 mm
Converging nozzle length	20 mm
Duct DIAMETER	25 mm
Duct length	Varies from 1D to 6D
Rib width	3 mm
Rib height	1 mm

A comparison between the numerical results and the previous Rathakrishnan's experimental data (Rathakrishnan [29]) was performed on a controlled model on ribs with an aspect ratio of 3:1. It was determined that for a duct with five 3:1 aspect ratio, ribs resulted in a good agreement as depicted in Figures 5(a) to (d). The percentage error was below 5%, ensuring the method's reliability. While isentropic flow theory suggests that sonic conditions should be achieved at the nozzle exit for a primary pressure ratio of 1.89, real-world flows are inherently viscous and non-isentropic. From this, minor discrepancies occur, which can be considered acceptable. Moreover, the complex nature of compressible flow at sonic Mach numbers, characterized by shock waves and nonlinear behavior, can also contribute to slight variations in base pressure. Backflow and boundary layer effects at different L/D ratios may further influence these variations.

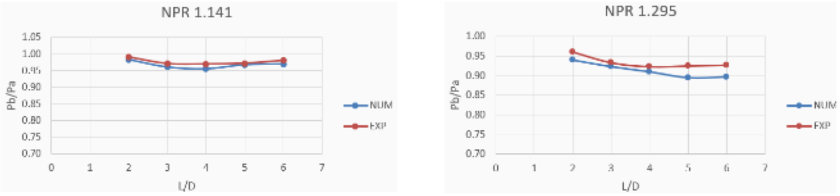

(a) NPR 1.141

(b) NPR 1.295

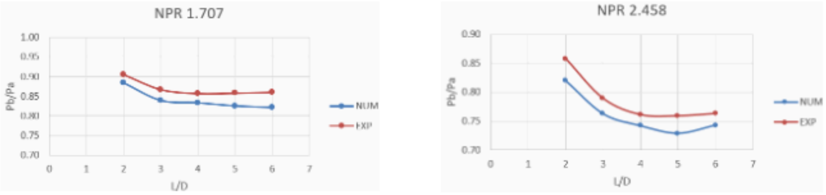

(c) NPR 1.707

(d) NPR 2.458

Figure 5. Graph of results validation at specific NPR.

3.6. Mesh independence study

The Mesh Independence Study (MIS) aims to determine the optimal mesh size for precise simulations that require shorter computational times without incurring excessive expenses. It considered multiple mesh configurations, ranging from coarsest to finest, with a progressive increase in the number of nodes and elements, as shown in Table 4. The node and element counts were minimal in the coarsest mesh, reducing computational cost but leading to numerical diffusion and less accurate base pressure predictions. Flow separation and recirculation regions were not accurately captured, which affected the accuracy of the passive control analysis.

As the mesh was refined to a medium level, the number of nodes and elements increased, improving the resolution of flow structures. Base pressure predictions became more stable, exhibiting less variation than those on the coarsest mesh. Flow separation and reattachment regions became more distinct, providing a better understanding of the passive control mechanism while minimizing computational cost. Further refinement led to a finer mesh, where velocity and pressure gradients were more accurately resolved. Base pressure predictions approached converged values with minimal variation compared to the medium mesh, ensuring reliable results. Flow structures, shock interactions, and turbulence effects were well captured, contributing to improved simulation accuracy.

The finest mesh contained the highest number of nodes and elements, but its results remained nearly identical to the fine mesh, confirming mesh independence. No substantial improvement in accuracy was observed, but the computational cost increased drastically.

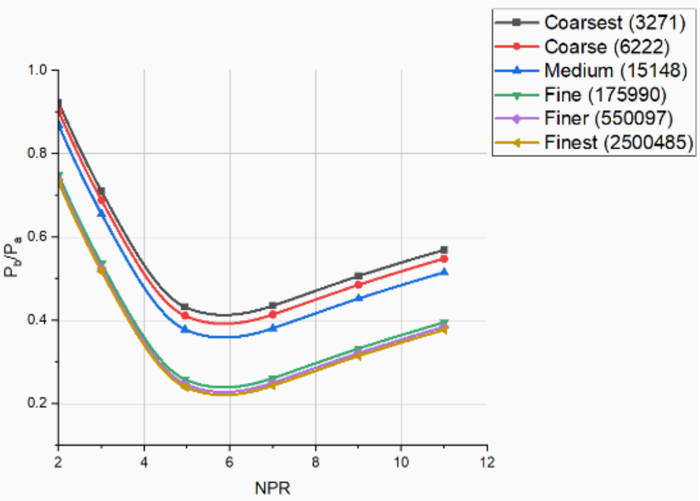

Figure 6. Results of mesh check.

The outcome of the MIS indicated that the base pressure converged beyond a certain refinement level, demonstrating that further mesh refinement did not significantly impact the results. The optimal mesh was selected based on a balance between accuracy and computational efficiency, typically favoring the fine or finer mesh, as illustrated in Figure 6.

Table 4. Mesh independence study

Element size	Coarsest	Coarse	Medium	Fine	Finer	Finest
Nodes	3432	6452	15614	176755	553495	2508903
Elements	3271	6222	15148	175990	550097	2500485

4. Results and Discussion

4.1. Contour plot for $L/D = 6$ at 1D location, without rib

Figures 7(a) to (d), respectively, show the pressure, velocity, temperature, and turbulence kinetic energy at $NPR = 3$. Since the nozzle is over-expanded and the rib radius is 1 mm, there is no appreciable change in these parameters, and they exhibit nearly the same patterns as discussed earlier.

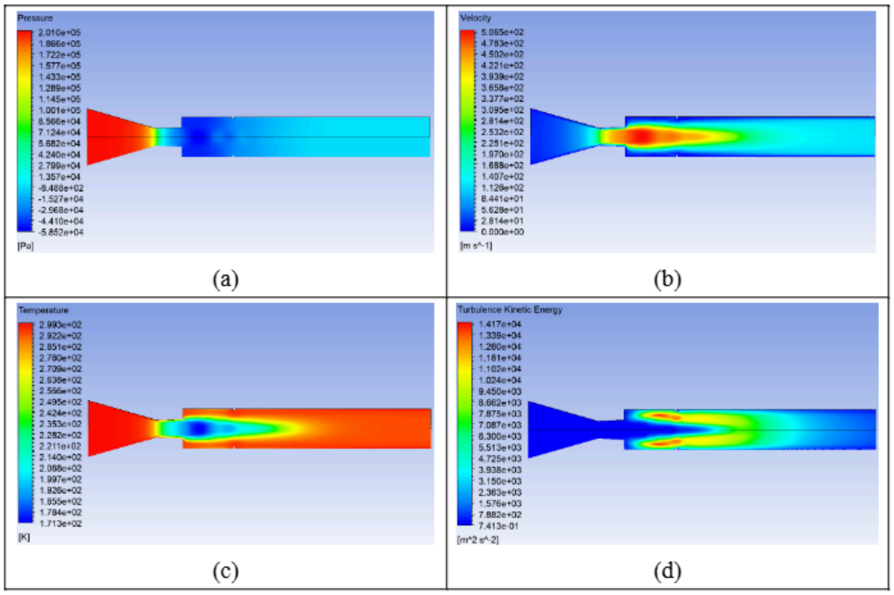

(a) (b)

(c) (d)

Figure 7. Contour plot for $L/D = 6$, 1 mm rib, and $NPR = 3$, where (a) pressure, (b) velocity, (c) temperature, and (d) turbulence kinetic energy.

Figures 8(a) to (d), respectively, show the contours for pressure, velocity, temperature, and turbulence kinetic energy. In Figure 8(a), as the flow is perfectly expanded, Mach waves will form, and due to the increase in duct area, this will result in low pressure. As far as velocity is concerned, low values are just near the wall. Still, fifty percent of the duct's length has high velocity. The temperature in the diverging part of the nozzle attains low values, and this trend continues till forty percent of the duct. Later, the temperature recovers. Similarly, the turbulence kinetic energy also has low values due to the nozzle being perfectly expanded; later, beyond fifty percent of the duct's length, turbulence kinetic energy recovery occurs.

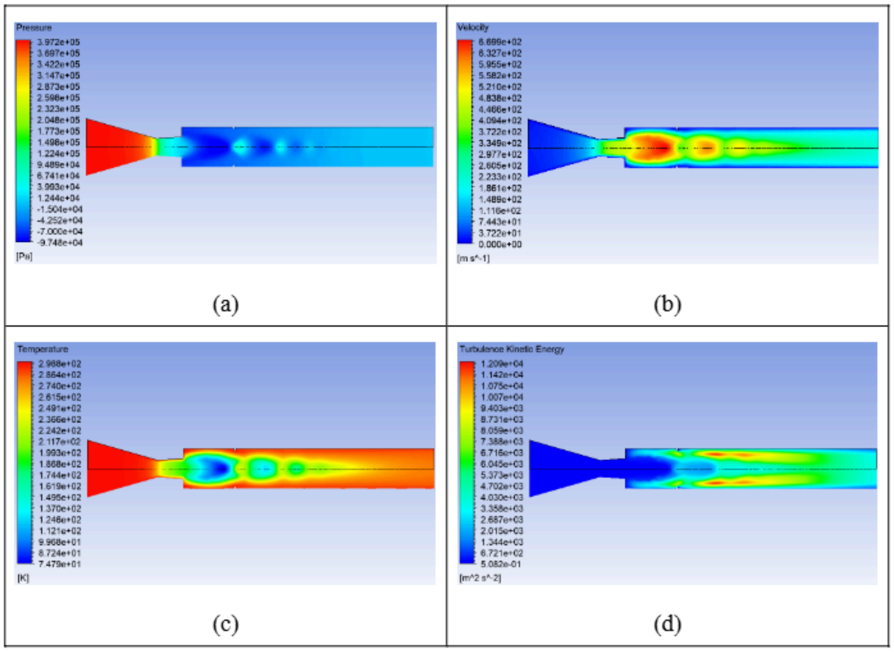

(a) (b)

(c) (d)

Figure 8. Contour plot for $L/D = 6,$ 1 mm rib, and $NPR = 4.95,$ where (a) pressure, (b) velocity, (c) temperature, and (d) turbulence kinetic energy.

Figures 9(a) to (d), respectively, show the contours for pressure, velocity, temperature, and turbulence kinetic energy. In Figure 9(a), the nozzle is under-expanded. At a level of under-expansion of 1.42 (i.e., $P_e/P_a = 1.42$), an expansion fan will be present, and the flow will expand beyond being exhausted into a larger space. That will cause a decrease in pressure inside the duct, as is evident in the results. As far as velocity is concerned, low values are just near the wall. Still, ninety percent of the length of the duct has high velocity. The temperature in the diverging part of the nozzle attains low values, and this trend continues till ninety percent of the duct. Later, the temperature recovers. Similarly, the turbulence kinetic energy also has low values due to the nozzle being under-expanded. This condition persists until beyond seventy percent of the duct length, where turbulence kinetic energy recovery occurs.

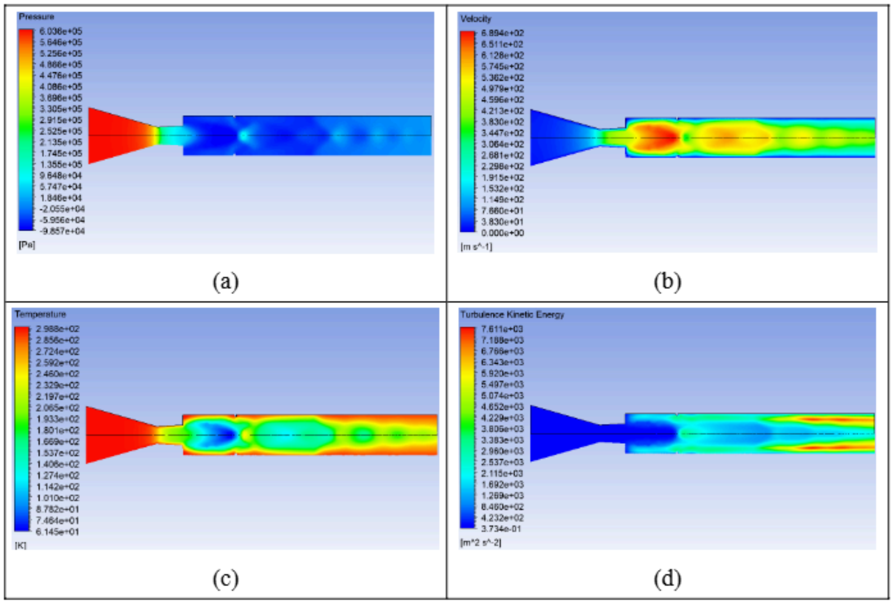

(a) (b)

(c) (d)

Figure 9. Contour plot for $L/D = 6$, 1 mm rib, and $NPR = 7$, where (a) pressure, (b) velocity, (c) temperature, and (d) turbulence kinetic energy.

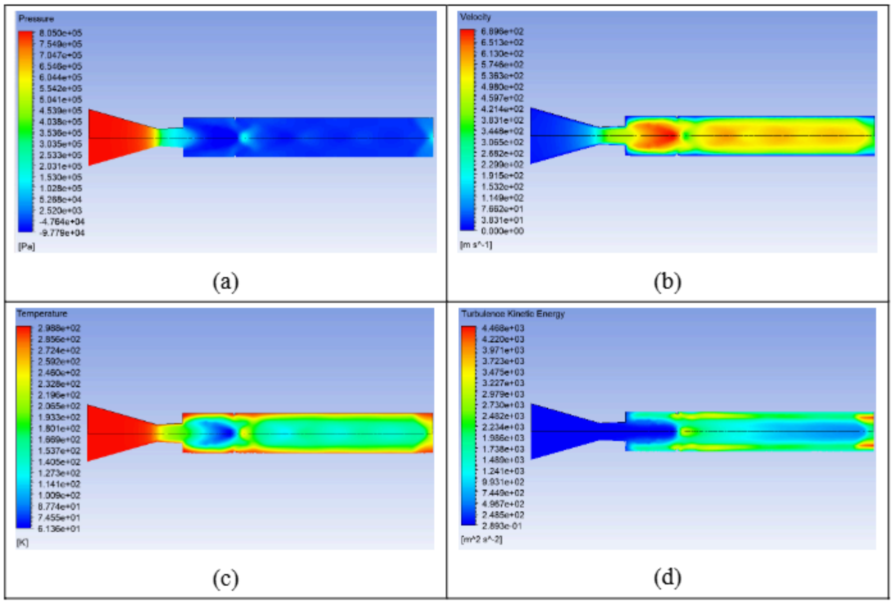

(a) (b)

(c) (d)

Figure 10. Contour plot for $L/D = 6,$ 1 mm rib, and $NPR = 9,$ where (a) pressure, (b) velocity, (c) temperature, and (d) turbulence kinetic energy.

Figures 10(a) to (d), respectively, show the contours for pressure, velocity, temperature, and turbulence kinetic energy at $NPR = 9$ when a 1 mm rib radius is placed. In this case, NPR has further increased, resulting in a higher level of under-expansion. In Figure 10(a), as this is under-expanded and the level of under-expansion is 1.82 (i.e., $P_e/P_a = 1.82$), the increased level of under-expansion will result in high velocity inside the duct. The length of the duct has high velocity. The temperature in the diverging part of the nozzle attains low values, and this trend continues till ninety percent of the duct. Later, the temperature recovers. Similarly, the turbulence kinetic energy also has low values due to the nozzle being under-expanded. This condition persists until beyond seventy percent of the duct length, where turbulence kinetic energy recovery occurs.

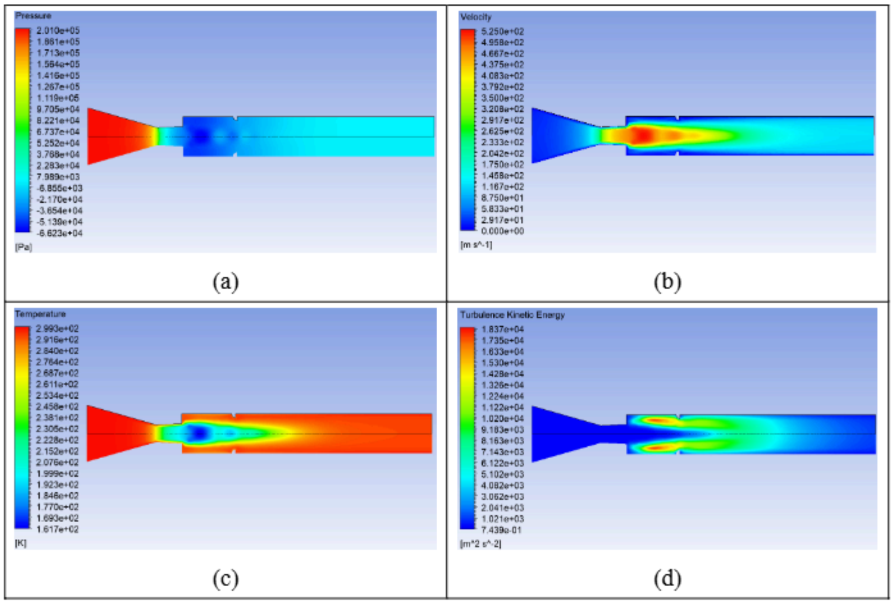

Figure 11. Contour plot for $L/D = 6,$ 2 mm rib, and $NPR = 3,$ where (a) pressure, (b) velocity, (c) temperature, and (d) turbulence kinetic energy.

Figures 11(a) to (d), respectively, show the contours for pressure, velocity, temperature, and turbulence kinetic energy for $L/D = 6,$ $NPR = 3,$ and 2 mm rib radius. In Figure 11(a), as this is over-expanded and the level of under-expansion is 0.61 (i.e., $P_e/P_a = 0.61$), there will be an oblique shock wave. The pressure increases until it becomes equal to the ambient pressure, apart from being exhausted into a larger area, which causes a decrease in the pressure inside the duct, as shown in the figure. As far as velocity is concerned, low values are just near the wall. Still, forty percent of the length of the duct has high velocity. The temperature in the diverging part of the nozzle attains low values, and this trend continues till forty percent in the central part of the duct. Later, the temperature recovers. Similarly, the turbulence kinetic energy also has low values due to the nozzle being over-expanded. This condition persists until beyond forty percent of the duct length, where turbulence kinetic energy recovery occurs.

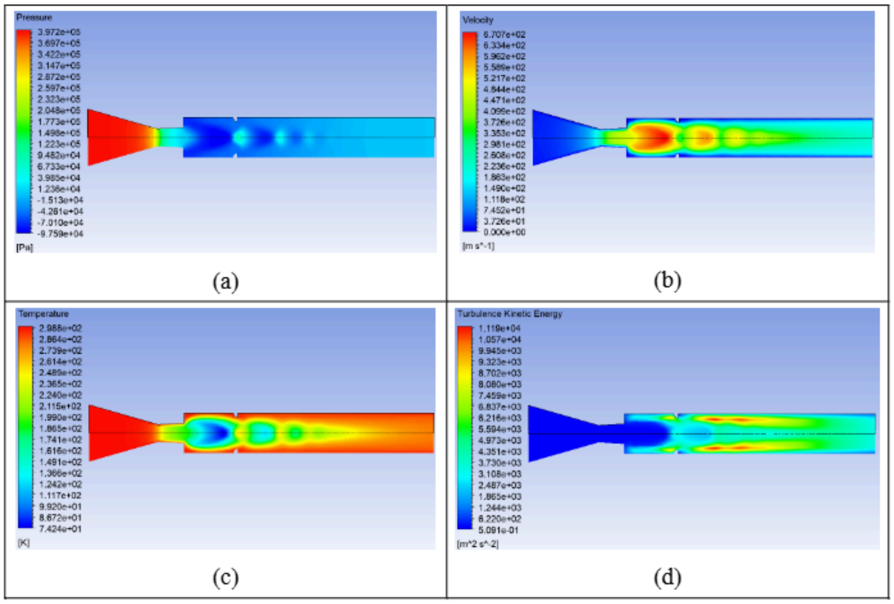

Figure 12. Contour plot for $L/D = 6,$ 2 mm rib, and $NPR = 4.95,$ where (a) pressure, (b) velocity, (c) temperature, and (d) turbulence kinetic energy.

Figure 12 shows similar results for $L/D = 6,$ rib radius = 2 mm, and $NPR = 4.94.$ Figure 12(a) shows a pressure contour that extends beyond the rib location as the duct correctly expands and Mach waves are formed, rather than oblique shock waves or expansion fans. Due to the sudden increase in the area, the velocity assumes low values near the wall; however, the primary jet contains high kinetic energy. Similarly, this assumes low values in the initial part of the duct and the primary jet. As far as the turbulent kinetic energy is concerned, its value is low inside the nozzle, and it persists for the primary part until twenty percent of the length.

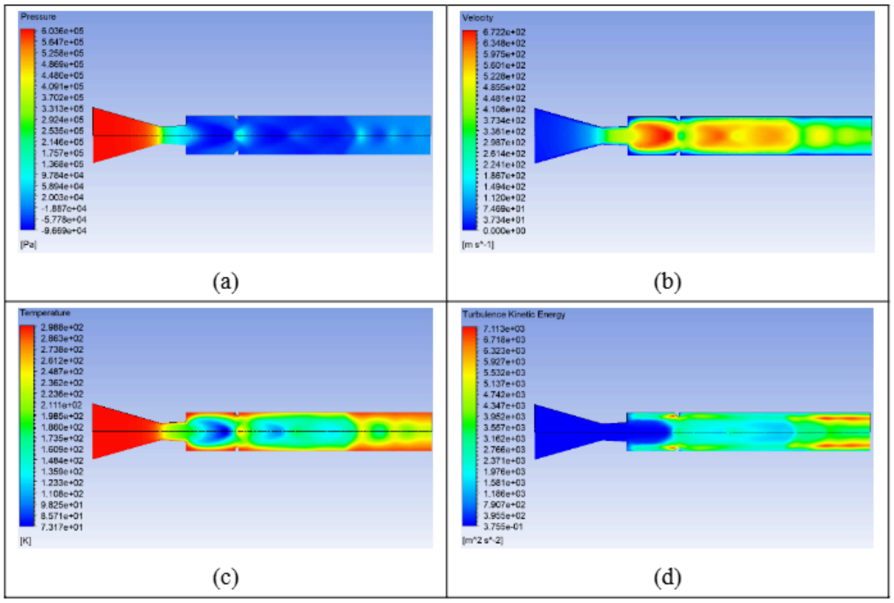

Figure 13. Contour plot for $L/D = 6$, 2 mm rib, and $NPR = 7$, where (a) pressure, (b) velocity, (c) temperature, and (d) turbulence kinetic energy.

Figure 13 shows similar results for $NPR = 7$; the rest of the parameters are the same. This figure reflects the effect of expansion levels. As the nozzle is under-expanded, the flow will further expand through the expansion fan; hence, a low-pressure contour is seen in Figure 13(a). Similarly, the velocity contour shows the increase in the velocity in the duct (Figure 13(b)). Likewise, the temperature takes lower values, as seen in Figure 13(c). Lastly, the turbulent intensity assumes lower values for short duct lengths but later increases.

Similar results for pressure, velocity, temperature, and turbulent intensity are observed, as seen in Figure 14 for $NPR = 7$. The only difference in this figure is that the NPR has increased from 7 to 9, and hence, the level of expansion has increased from 1.42 to 1.82.

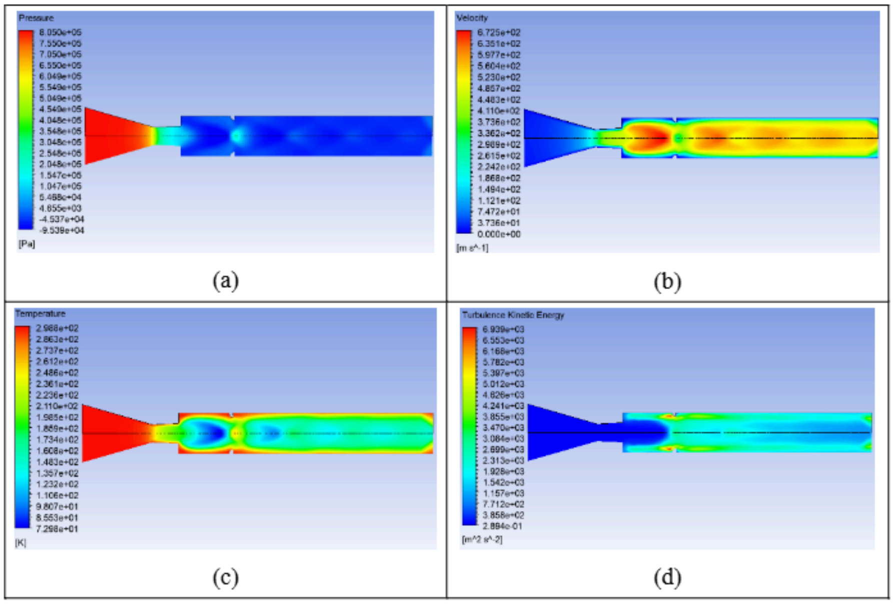

(a) (b)

(c) (d)

Figure 14. Contour plot for $L/D = 6$, 2 mm rib, and $NPR = 9$, where (a) pressure, (b) velocity, (c) temperature, and (d) turbulence kinetic energy.

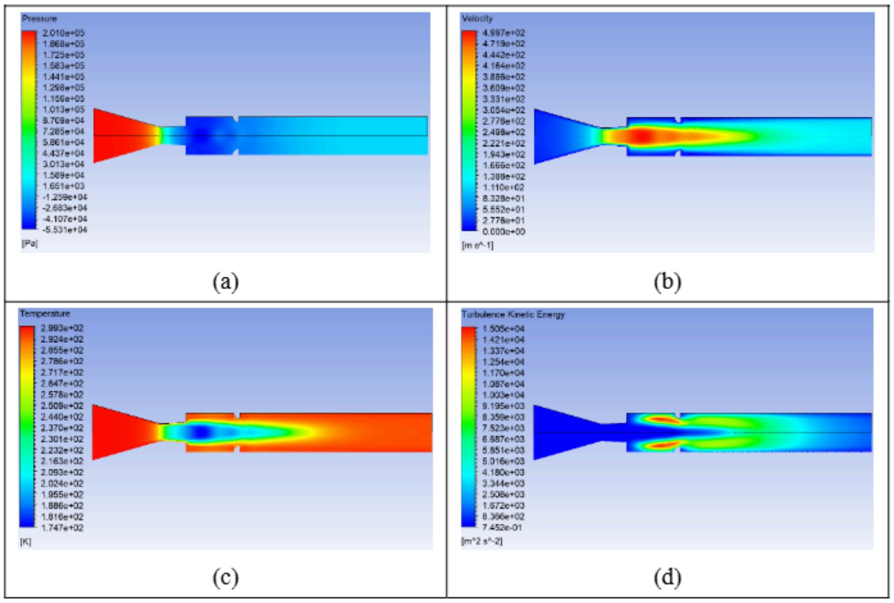

(a) (b)

(c) (d)

Figure 15. Contour plot for $L/D = 6$, 3 mm rib, and $NPR = 3$, where (a) pressure, (b) velocity, (c) temperature, and (d) turbulence kinetic energy.

Figure 15 shows the pressure, velocity, temperature, and turbulence kinetic energy contours for $L/D = 6$, rib radius = 3 mm, and NPR is 3. Here, the nozzle is over-expanded. Due to the rise in the rib radius, the flow exiting from the nozzle will face the rib of maximum radius and will block flow. Accordingly, the pressure, velocity, temperature, and turbulence kinetic energy will be modified.

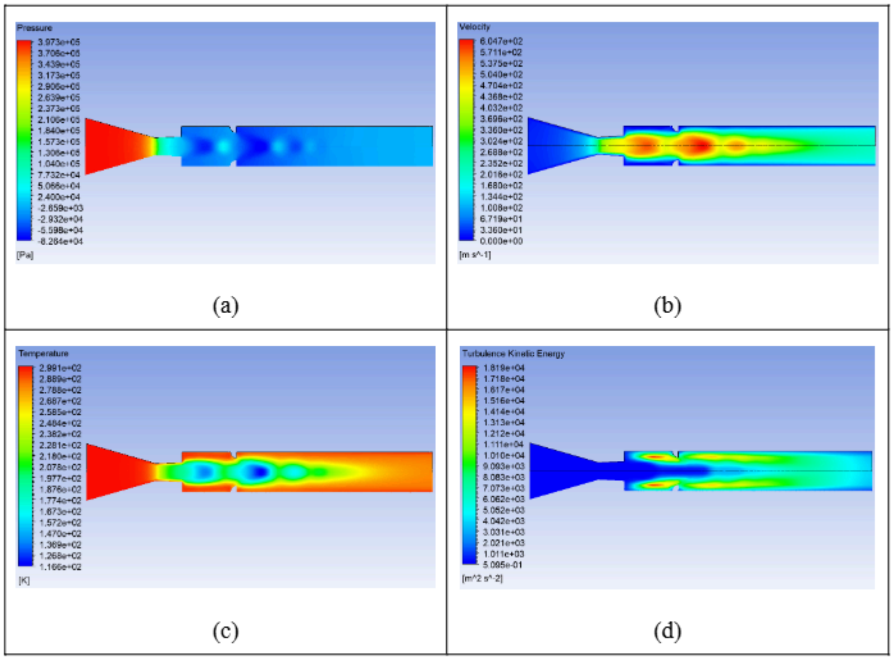

(a) (b)

(c) (d)

Figure 16. Contour plot for $L/D = 6$, 3 mm rib, and $NPR = 4.95$, where (a) pressure, (b) velocity, (c) temperature, and (d) turbulence kinetic energy.

Figure 16 shows the results of pressure, velocity, temperature, and kinetic energy for the ideally expanded nozzle. Here, due to the presence of the Mach waves, we will have marginal changes in the flow parameters.

Figures 17 and 18 show similar trends, with increase in NPR values of 7 and 9. This expansion results in lower pressure, higher velocity, lower temperature, and higher kinetic energy.

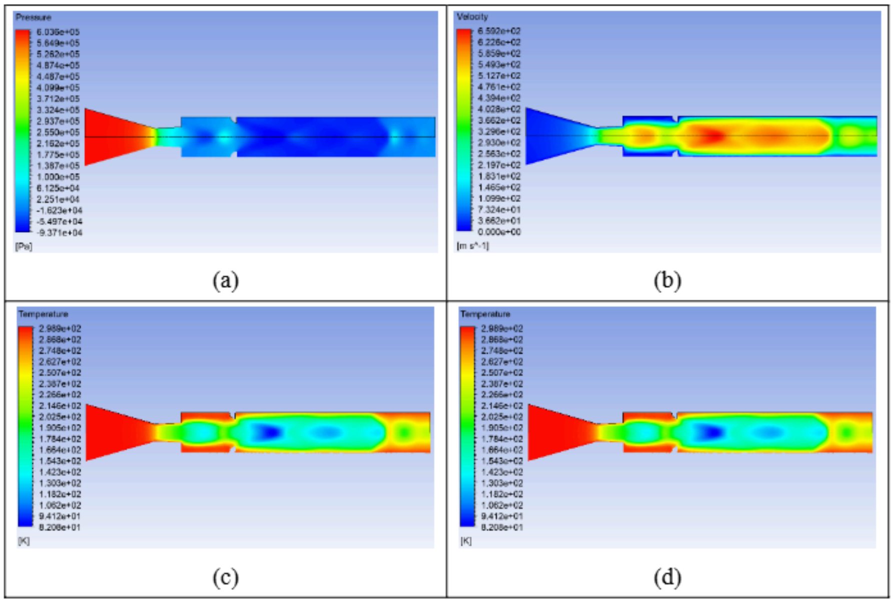

(a) (b)

(c) (d)

Figure 17. Contour plot for $L/D = 6$, 3 mm rib, and $NPR = 7$, where (a) pressure, (b) velocity, (c) temperature, and (d) turbulence kinetic energy.

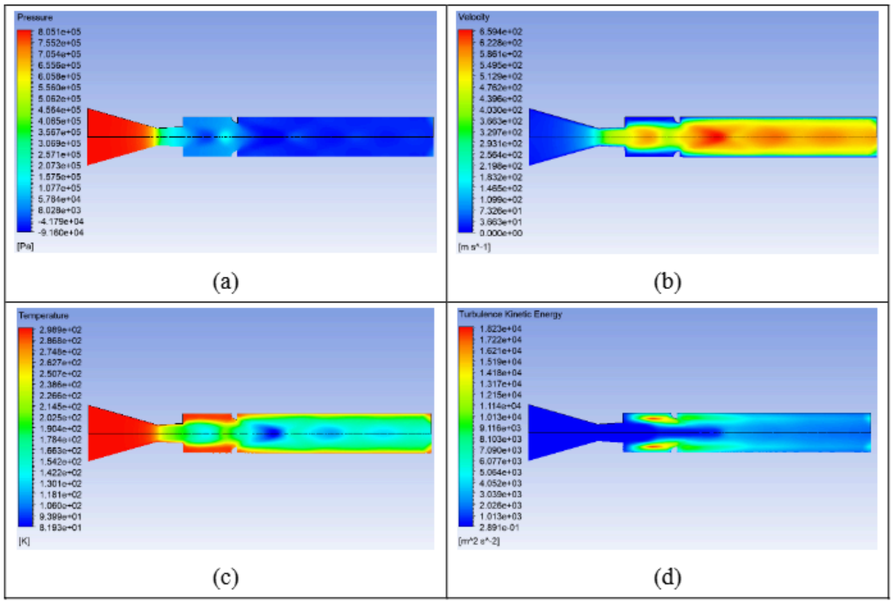

(a) (b)

(c) (d)

Figure 18. Contour plot for $L/D = 6$, 3 mm rib, and $NPR = 9$, where (a) pressure, (b) velocity, (c) temperature, and (d) turbulence kinetic energy.

4.2. Analysis of base pressure for rib facing the flat part of the rib

Figure 19 shows orientation 2 of the rib, where, when the flow exits from the nozzle into the enlarged duct, the shear layer faces the rib's flat and sharp corner. In this section, we will discuss the impact of the rib orientation on the flow field inside the duct and the control effectiveness of the passive control at supersonic Mach numbers, considering various expansion levels, rib geometries, and duct sizes.

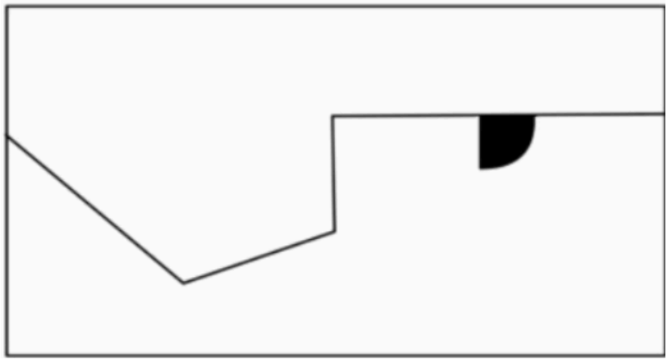

Figure 19. Quarter circular rib in orientation 2.

Base pressure analysis for $L/D = 1$, orientation 2

Figure 20 shows the outcomes of the present study for orientation 1 with duct length-to-diameter ratio $L/D = 1$ at NPR ranging from 3 to 11 for rib placement at $L/D = 0.5$ for rib radii 1 mm, 2 mm, and 3 mm. The results show that when the control is absent, the base pressure value continuously decreases until NPR 7; for NPRs greater than 7, an increase in the base pressure is observed. In normal circumstances, once the operating NPR exceeds the NPR required for correct expansion, there will be an increase in the base pressure. It is usually observed that when the relief available to the flow exceeds a specific limit, the shear layer exiting from the nozzle will reattach to the duct at a location beyond the optimum reattachment length. This will render the control ineffective, even when the jets are under-expanded. That may be why the base pressure reduction occurs at $NPR = 7$ instead of at $NPR = 5$. When the control is employed with rib radii 1 mm, 2 mm, and 3 mm, the base pressure ratios are 0.75, 0.9, and 1.19. When we compare the base pressure ratios with control and without control, it is seen that there is a considerable increase in the base pressure; however, it is still not equal to the atmospheric pressure, except for the rib radius of 3 mm.

Furthermore, it is seen that there are oscillations. One of the reasons for this pattern is that the rib is located very close to the nozzle exit, and the shear layer has not yet been attached. If the rib is located near the reattachment, then the rib will become effective.

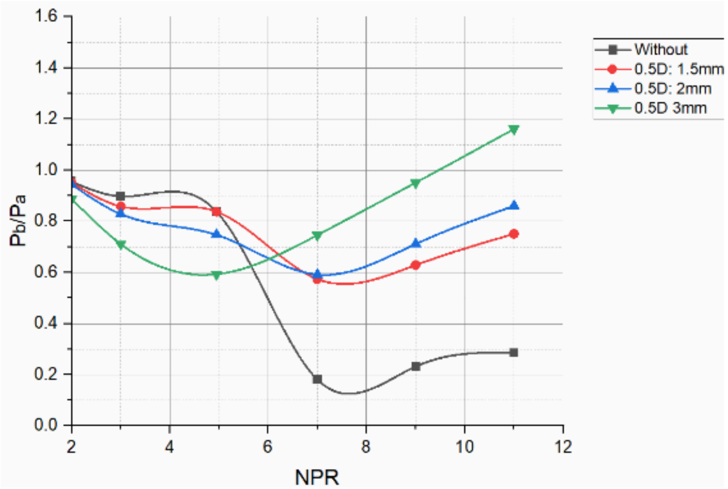

Figure 20. Base pressure vs. NPR for various rib size at 0.5D location for $L/D = 1$.

4.3. Base pressure analysis for $L/D = 2$, orientation 2

Figure 21 shows the outcomes of the current study, the base ratio vs. NPR with and without control for duct size $L/D = 2$ and rib radii 1.5 mm and 3 mm when located at $L/D = 0.5,\ 1.0$, and 1.5. As expected, a small rib radius of 1.5 mm will have minimal influence when the quarter rib control cannot impact the duct's flow field. However, the base pressure ratios are 0.8, 0.5, and 0.5. These results show that there is no definite pattern as far as base pressure is concerned. The physics behind this phenomenon involves the flow blockage due to the rib radius, the shock strength at the nozzle lip, the shock incident on the duct wall, and its reflection, resulting in a complex flow field that complicates the flow inside the duct. These ribs will be helpful if the mission requires raising the base pressure from the uncontrolled level to a fifty percent increase. For a larger increase in the base pressure by a hundred percent or more, a rib radius of 3 mm is the best option.

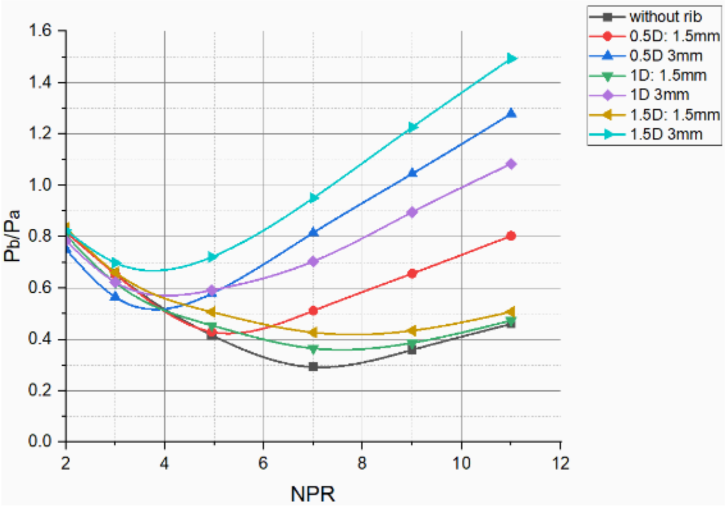

Figure 21. Base pressure vs. NPR for various rib sizes at various locations for $L/D = 2$.

Figure 21 shows that when the rib radius is 3 mm and placed at $L/D = 0.5,\ 1.0,\ 1.5,$ the maximum gain is seen for rib location at $L/D = 1.5,$ and the base pressure ratio is 1.5. It is also seen that a 3 mm rib located at $L/D = 0.5$ is more effective than the rib placed at $L/D = 1,$ even though at lower NPRs, the rib placed at $L/D = 1$ was more effective than at $L/D = 0.5.$ Once the nozzle is operated for NPR more than needed for correct expansion, the rib located at $L/D = 0.5$ is more effective than at $L/D = 1.0.$ These results reiterate that the flow field is highly complex and varies with changes in the NPR, expansion level, and shock strength.

4.4. Base pressure analysis for $L/D = 3$, orientation 2

Figure 22 presents the findings of the current study for duct $L/D = 3$ at various expansion levels and rib locations, specifically at $L/D = 0.5$, 1.0, 1.5, and 2.0 for rib radii of 1.5 and 3 mm. In these results, there are two clusters of base pressure, one for a rib radius of 1.5 mm and the other for a rib radius of 3 mm. When the passive control in the form of the quarter rib of radius 3 mm is employed, there is a progressive increase in the base pressure ratios, and they are 1.9, 1.6, 1.1, and 1.5 for the ribs located at $L/D = 2.0$, 1.5, 1.0, and 0.5. It is observed that the base pressure ratio for rib locations at $L/D = 1$ is lower than that for rib locations at 0.5. That is a peculiar case. It might be due to the reattachment length and strength of shock waves at $NPR = 11$. Hence, the flow field is dominated by compression and expansion waves; it is very complex in the duct, and one cannot generalize the flow pattern.

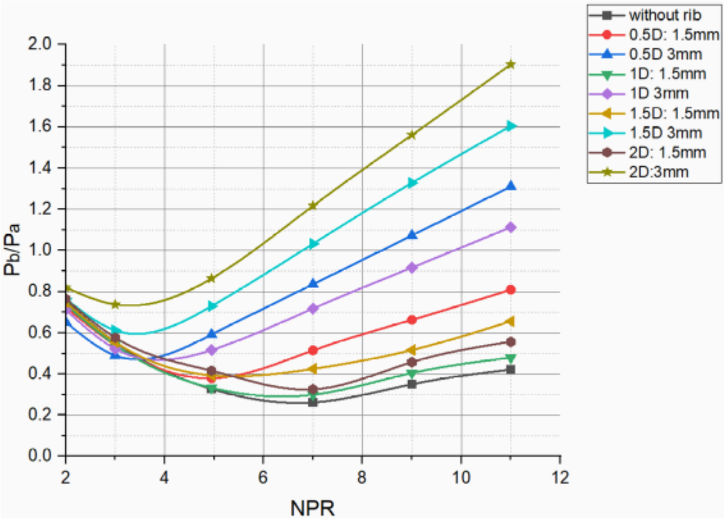

Figure 22. Base pressure vs. NPR for various rib sizes at various locations for $L/D = 3$.

Similarly, the 1.5 mm rib radius base pressure ratios show a different pattern. The base pressure ratios are 0.58, 0.65, 0.5, and 0.8 for rib locations at $L/D = 2.0,\ 1.5,\ 1.0,$ and 0.8. For this cluster, the most efficient rib location seems to be when placed at $L/D = 0.5.$ For other rib locations, these results show an erratic pattern; hence, one needs to analyze the base pressure results on a case-by-case basis.

4.5. Base pressure analysis for $L/D = 4$

Figure 23 presents the outcomes of this study for the duct length-to-diameter ratio $(L/D = 4)$ and rib orientation 2, with rib radii of 1.5 mm and 3 mm, for rib locations at L/D ratios of 0.5, 1.0, 1.5, 2.0, and 3.0, at various expansion levels. When the rib radius is 3 mm, the base pressure ratio ranges from 2.6, 1.9, 1.5, 1.1, and 1.3 for rib locations at $L/D = 3.0,\ 2.0,\ 1.5,\ 1.0,$ and 0.5. The outcomes for the 3 mm rib radius increase with a progressive shift of the control mechanism towards the leading edge, except at the rib location of $L/D = 1.0.$ The base pressure ratio at $L/D = 1.0$ is lower than that at $L/D = 0.5,$ possibly due to the position of the reattachment point and the strength of the waves at these positions.

As far as the lower rib radius of 1.5 mm is concerned, it results in the normalized base pressure 0.7, 0.6, 0.5, 0.4, and 0.9 for rib locations at $L/D = 3.0,\ 2.0,\ 1.5,\ 1.0,$ and 0.5. From the results, it is seen that there is a decrease in the base pressure ratio with a shift in the location of the rib from $L/D = 3$ to 0.5. For the lowest rib radius, there is maximum gain in the base pressure. Apart from this location, a pattern is set by the control mechanism. For some locations of the ribs, the base pressure ratios are the same or equal to those without control values. This behavior can be attributed to the strength of the shock waves, expansion level, duct size, rib size, and rib locations. Here, every parameter plays a significant role. Hence, one must study them carefully before finalizing the rib size and location.

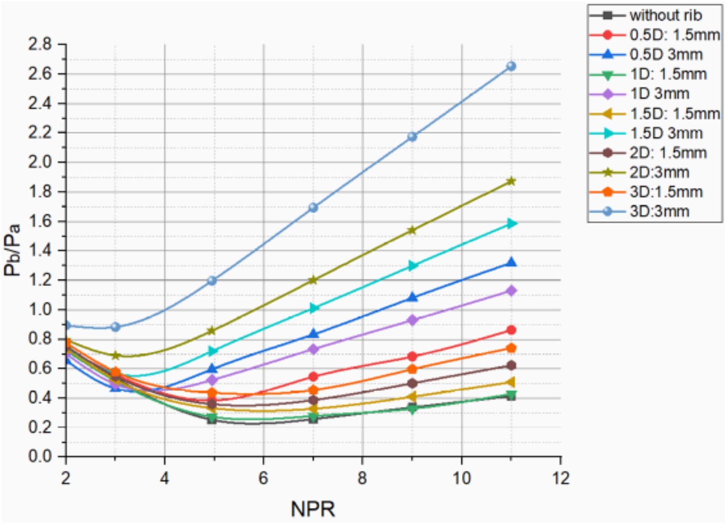

Figure 23. Base pressure vs. NPR for various rib sizes at various locations for $L/D = 4$.

4.6. Base pressure analysis for $L/D = 5$

Base pressure analysis for $L/D = 5,$ orientation two as a function of nozzle pressure ratio for rib radii 1.5 mm and 3 mm for rib locations $L/D = 0.5,\ 1.0,\ 1.5,\ 2.0,$ and 3.0 are shown in Figure 24. As discussed earlier for this case, the results are similar as seen for lower duct lengths except with the minor changes for some rib locations. Slight changes in the base pressure ratios are also seen for the change in the duct diameter. For smaller duct sizes, the influence of ambient pressure is maximum; however, with a progressive increase in duct size, variations in base pressure become visible for rib locations at $L/D = 2$ and 3.

These results show that for a rib radius of 3 mm, the base pressure ratios are 2.6, 1.9, 1.5, 1.1, and 1.3 when ribs are placed at $L/D = 3,\ 2,\ 1.5,\ 1,$ and 0.5. There are marginal changes in the base pressure values for the above reasons. The same applies to a lower rib radius of 1.5 mm. Passive control is marginally effective, and if the mission requirement is to enhance the base pressure ratio by 50 percent, then a 1.5 rib radius is the right choice when placed at $L/D = 0.5$. We may also put them at other locations based on mission requirements.

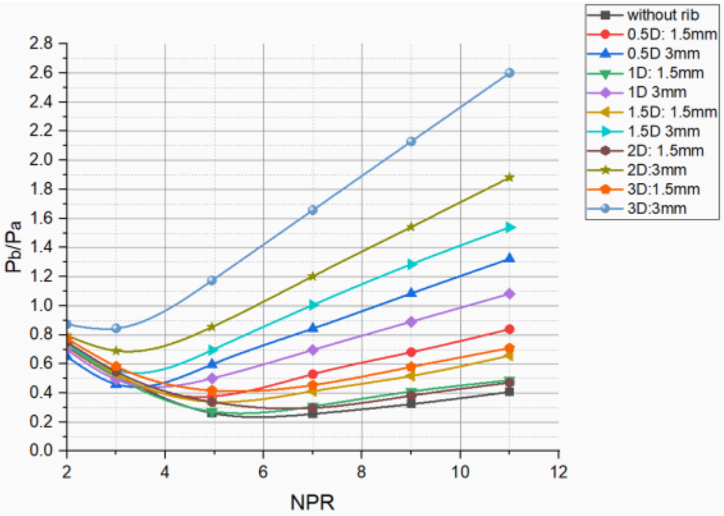

Figure 24. Base pressure vs. NPR for various rib sizes at various locations for $L/D = 5$.

4.7. Base pressure analysis for $L/D = 6$

For the highest duct length (i.e., $L/D = 6$), the outcomes of the present study are depicted in Figure 25 for various expansion levels, rib radii, and rib locations. The results can be divided into two groups, with two rib radii of 1.5 mm and 3 mm. Regarding base pressure for a 3 mm radius, there is a progressive increase in base pressure when the control mechanism is shifted from $L/D = 0.5$ to 3. The corresponding base pressure ratios are 2.7, 2.0, 1.7, and 1.3, except that the results are identical for rib locations at $L/D = 0.5$ and 1.0. Regarding the lower rib radius of 1.5 mm, the base pressure ratios are 0.65, 0.5, 0.52, 0.65, 0.6, and 0.79 for rib located at $L/D = 3$, 2, 1.5, 1, and 0.5. For the smallest rib radius, there is a maximum gain in the base pressure.

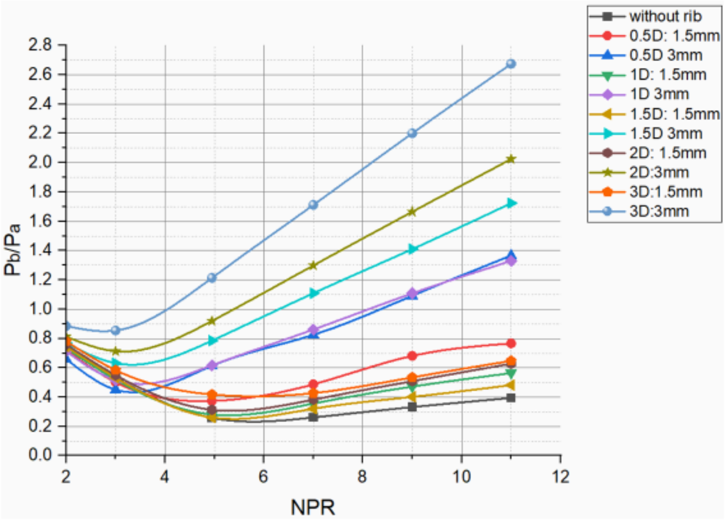

Figure 25. Base pressure vs. NPR for various rib sizes at various locations for $L/D = 6$.

4.8. Contour plot for $L/D = 6$ at 1D location

Figure 26 shows the contour plots for $L/D = 6$, rib radius of 1 mm, and $NPR = 3$. As the nozzle is over-expanded, this level of over-expansion results in a marginally increased pressure, lower velocity, higher temperature, and a recirculation bubble at the nozzle exit due to flow separation.

Figure 27 shows the contour plots for $L/D = 6$, rib radius of 1 mm, and $NPR = 4.95$. As the nozzle is correctly expanded, this results in the formation of Mach waves, with nearly the same pressure and velocity at correct expansion, a higher temperature, and a weak recirculation bubble at the nozzle exit due to flow separation.

Figure 28 shows the contour plots for $L/D = 6$, rib radius of 1 mm, and $NPR = 7$. As the nozzle is under-expanded, this results in the formation of expansion waves, a lower pressure due to the expansion of the jet, a higher velocity for the main jet, a lower temperature due to the expansion, and a weak recirculation bubble at the nozzle exit due to flow separation.

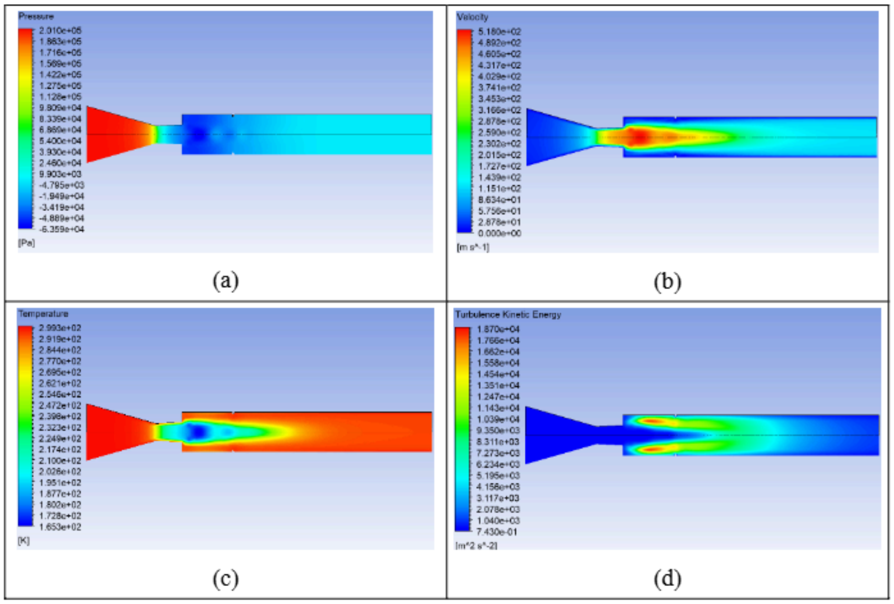

(a) (b)

(c) (d)

Figure 26. Contour plot for $L/D = 6$, 1 mm rib, and $NPR = 3$, where (a) pressure, (b) velocity, (c) temperature, and (d) turbulence kinetic energy.

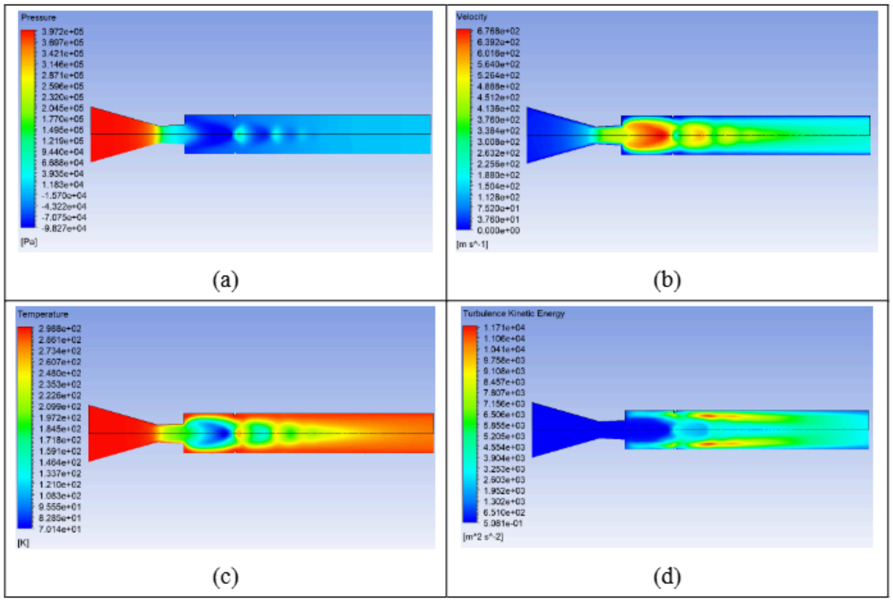

(a) (b)

(c) (d)

Figure 27. Contour plot for $L/D = 6$, 1 mm rib, and $NPR = 4.95$, where (a) pressure, (b) velocity, (c) temperature, and (d) turbulence kinetic energy.

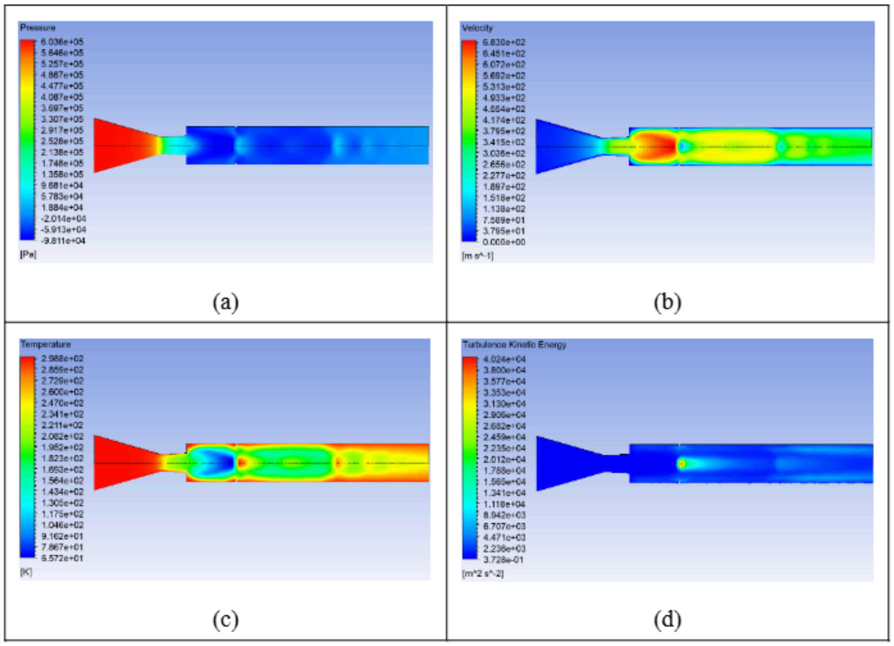

(a) (b)

(c) (d)

Figure 28. Contour plot for $L/D = 6$, 1 mm rib, and $NPR = 7$, where (a) pressure, (b) velocity, (c) temperature, and (d) turbulence kinetic energy.

Figure 29 shows the contour plots for $L/D = 6$, rib radius of 1 mm, and $NPR = 9$. As there is a further increase in the NPR and hence in the under-expansion level of nozzle, this results in formations of the expansion waves and nearly lower pressure due to the expansion of the jet, a higher velocity for the main jet, low temperature because of the expansion, and a weak recirculation bubble at the nozzle exit due to flow separation.

Figure 30 shows the contour plots for $L/D = 6$, rib radius of 2 mm, and $NPR = 3$. The NPR is low where the jet is over-expanded; this results in the formation of oblique shock waves and initially lower pressure due to the over-expansion of the jet, a lower velocity for the main jet, high temperature due to the over expansion, and a weak recirculation bubble at the nozzle exit resulting from flow separation.

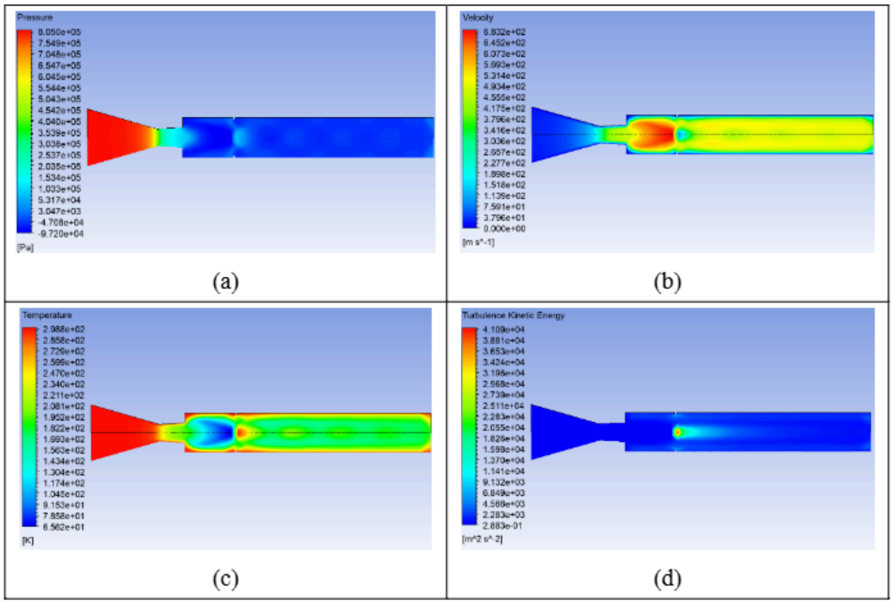

Figure 29. Contour plot for $L/D = 6$, 1 mm rib, and $NPR = 9$, where (a) pressure, (b) velocity, (c) temperature, and (d) turbulence kinetic energy.

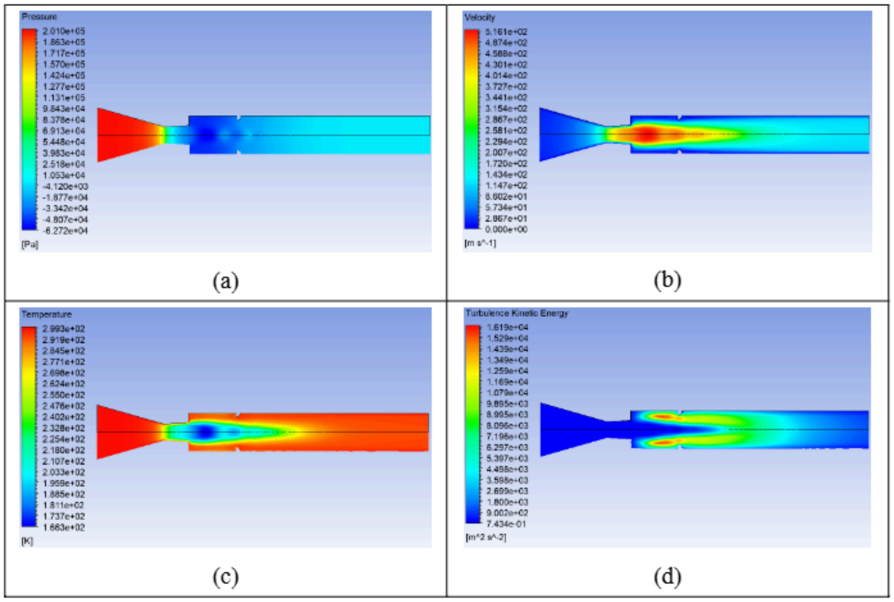

Figure 30. Contour plot for $L/D = 6$, 2 mm rib, and $NPR = 3$, where (a) pressure, (b) velocity, (c) temperature, and (d) turbulence kinetic energy.

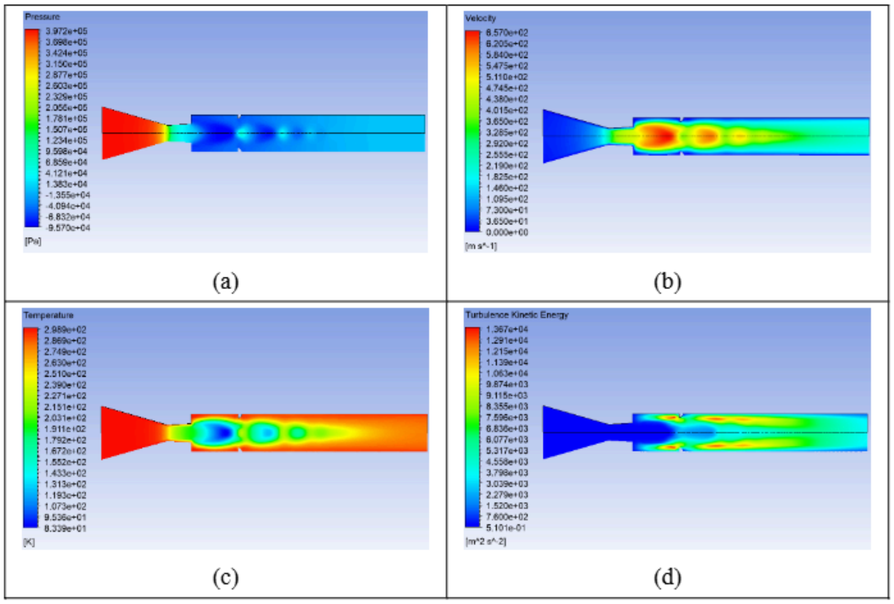

(a) (b)

(c) (d)

Figure 31. Contour plot for $L/D = 6$, 2 mm rib, and $NPR = 4.95$, where (a) pressure, (b) velocity, (c) temperature, and (d) turbulence kinetic energy.

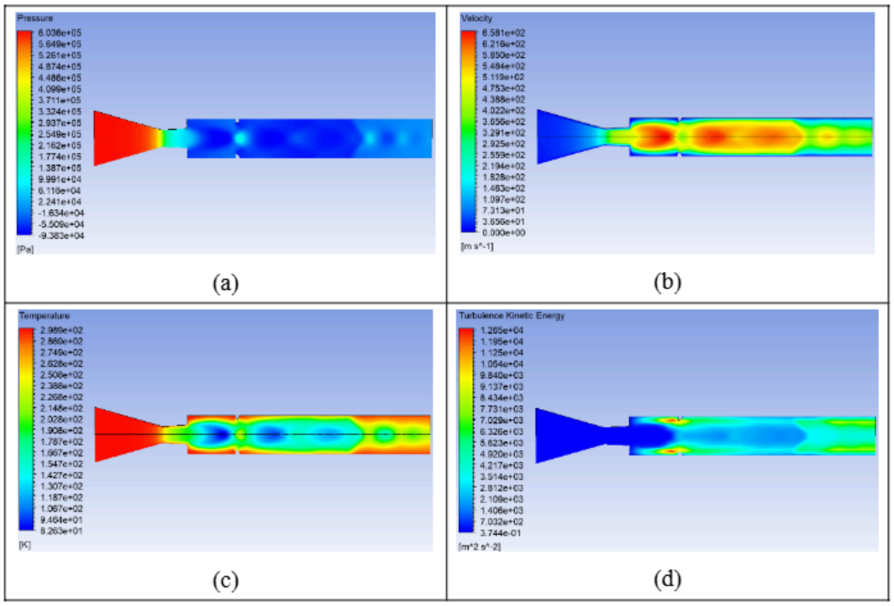

(a) (b)

(c) (d)

Figure 32. Contour plot for $L/D = 6$, 2 mm rib, and $NPR = 7$, where (a) pressure, (b) velocity, (c) temperature, and (d) turbulence kinetic energy.

Figure 31 shows the contour plots for $L/D = 6,$ rib radius of 2 mm, and $NPR = 4.95.$ As there is a further increase in the NPR and hence in the expansion level of nozzle, for this NPR, the nozzle is correctly expanded; this results in formations of the Mach waves and nearly lower pressure due to the expansion of the jet, a higher velocity for the main jet, low temperature because of the expansion, and a weak recirculation bubble at the nozzle exit due to flow separation.

Figure 32 shows the contour plots for $L/D = 6,$ rib radius of 2 mm, and $NPR = 7.$ As there is a further increase in the NPR and hence in the under-expansion level of nozzle having the value of 1.42, this results in formations of the expansion waves and nearly lower pressure due to the expansion of the jet, a higher velocity for the main jet, low temperature because of the expansion, and a weak recirculation bubble at the nozzle exit due to flow separation.

Figure 33 shows the contour plots for $L/D = 6,$ rib radius of 2 mm, and $NPR = 9.$ As there is a further increase in the NPR and hence in the under-expansion level of nozzle, this results in formations of the expansion waves and nearly lower pressure due to the expansion of the jet, a higher velocity for the main jet, low temperature because of the expansion, and a weak recirculation bubble at the nozzle exit due to flow separation.

Figure 34 shows the contour plots for $L/D = 6,$ rib radius of 3 mm, and $NPR = 3.$ The NPR is low where the jet is over-expanded; this results in the formation of oblique shock waves and initially lower pressure due to the over-expansion of the jet, a lower velocity for the main jet, high temperature due to the over-expansion, and a weak recirculation bubble at the nozzle exit resulting from flow separation.

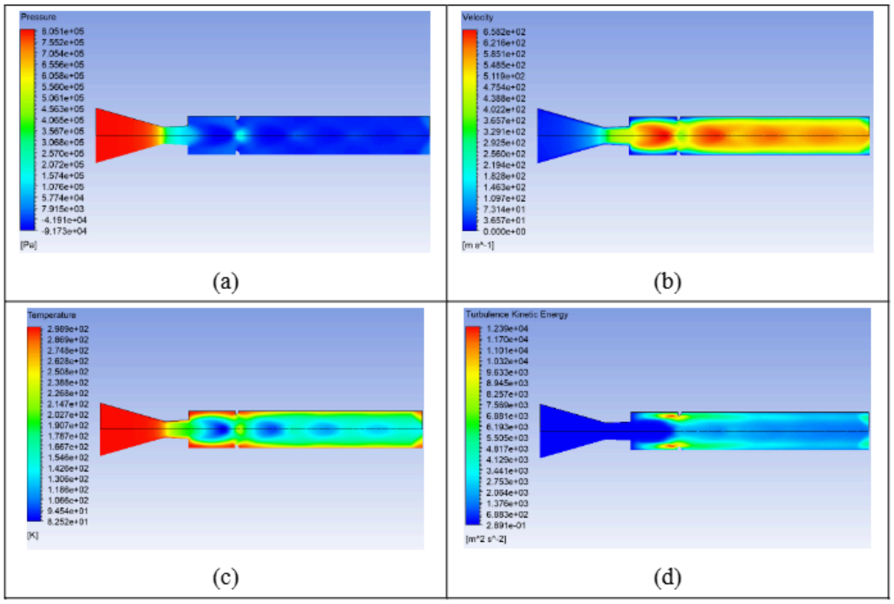

Figure 33. Contour plot for $L/D = 6,$ 2 mm rib, and $NPR = 9,$ where (a) pressure, (b) velocity, (c) temperature, and (d) turbulence kinetic energy.

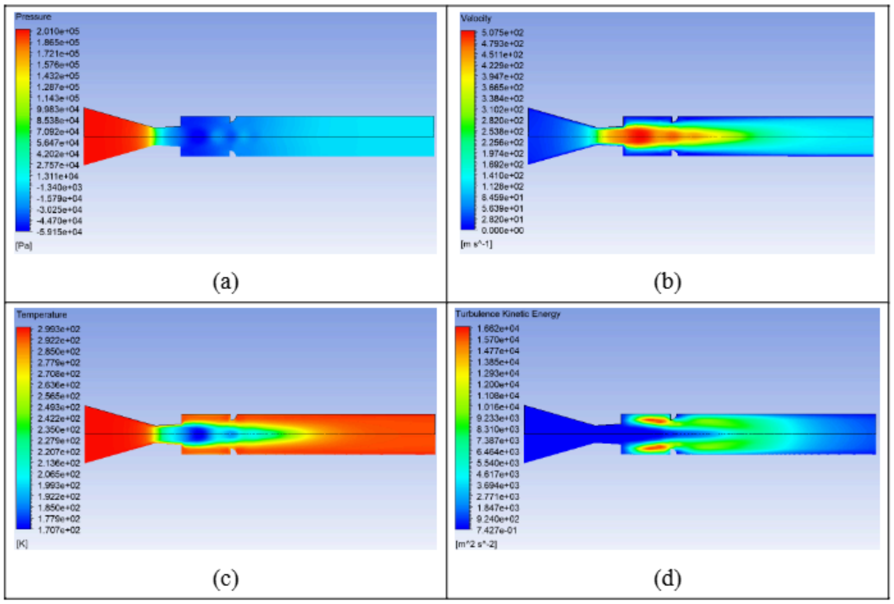

Figure 34. Contour plot for $L/D = 6,$ 3 mm rib, and $NPR = 3,$ where (a) pressure, (b) velocity, (c) temperature, and (d) turbulence kinetic energy.

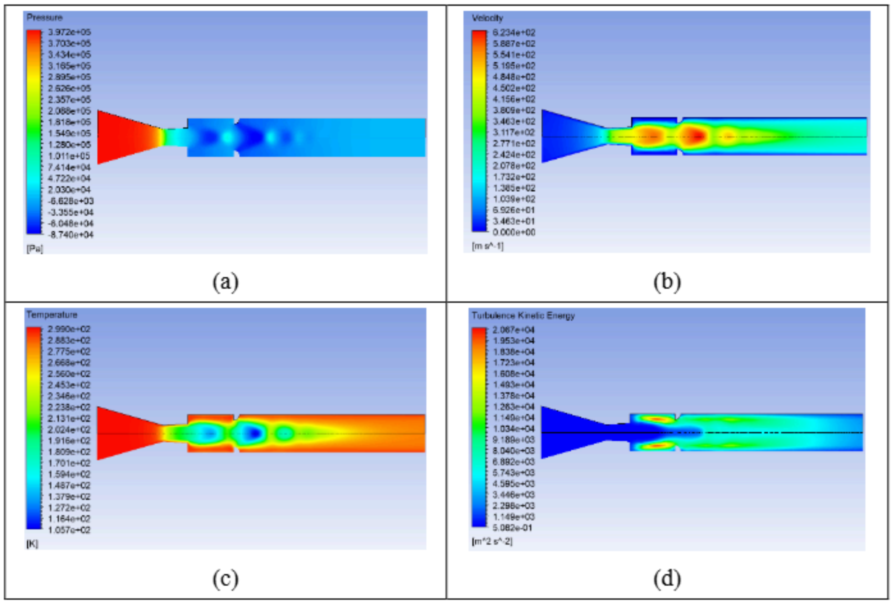

Figure 35. Contour plot for $L/D = 6$, 3 mm rib, and $NPR = 4.95$, where (a) pressure, (b) velocity, (c) temperature, and (d) turbulence kinetic energy.

Figure 35 shows the contour plots for $L/D = 6$, rib radius of 3 mm, and $NPR = 4.95$. The NPR is such that the jet is ideally expanded which results in the formation of Mach waves and initially constant pressure due to the correct expansion of the jet, a lower velocity for the main jet, greater temperature due to the over-expansion, and a weak recirculation bubble at the nozzle exit due to flow separation.

Figure 36 shows the contour plots for $L/D = 6$, rib radius of 2 mm, and $NPR = 7$. As there is a further increase in the NPR and hence in the under-expansion level of nozzle having the value of 1.42, this results in formations of the expansion waves and nearly lower pressure due to the expansion of the jet, a higher velocity for the main jet, low temperature because of the expansion, and a weak recirculation bubble at the nozzle exit due to flow separation.

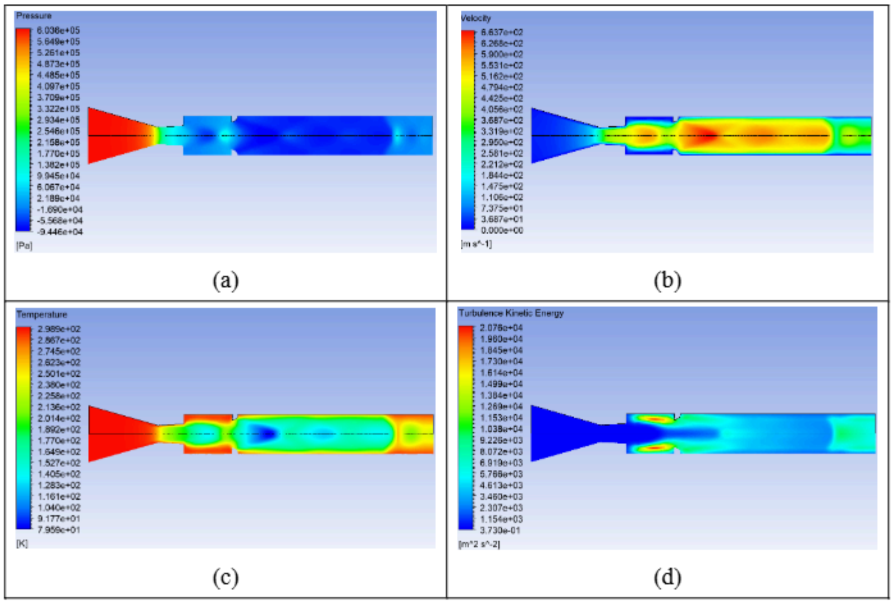

(a) (b)

(c) (d)

Figure 36. Contour plot for $L/D = 6$, 3 mm rib, and $NPR = 7$, where (a) pressure, (b) velocity, (c) temperature, and (d) turbulence kinetic energy.

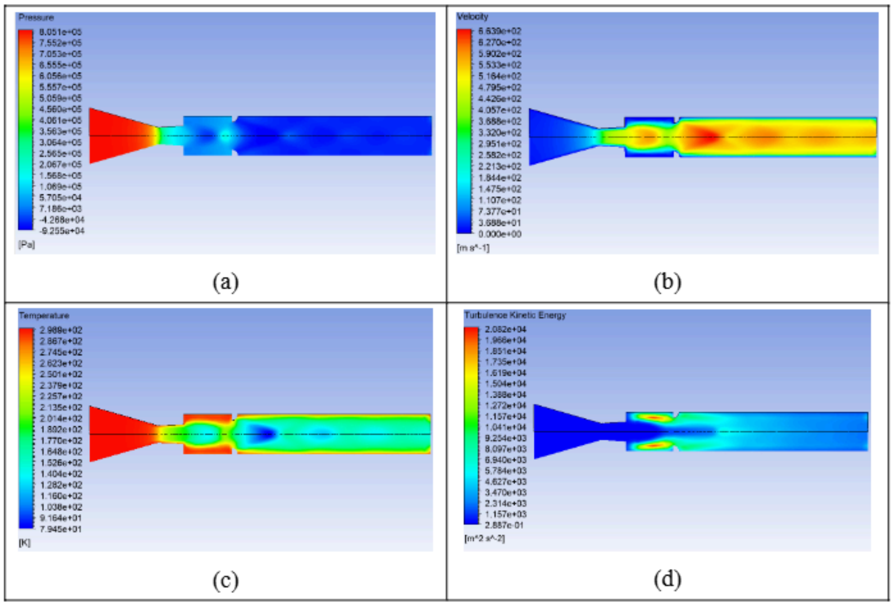

(a) (b)

(c) (d)

Figure 37. Contour plot for $L/D = 6$, 3 mm rib, and $NPR = 9$, where (a) pressure, (b) velocity, (c) temperature, and (d) turbulence kinetic energy.

Figure 37 shows the contour plots for $L/D = 6,$ rib radius of 3 mm, and $NPR = 9.$ As there is a further increase in the NPR and hence in the under-expansion level of nozzle, this results in formations of the expansion waves and nearly lower pressure due to the expansion of the jet, a higher velocity for the main jet, low temperature because of the expansion, and a weak recirculation bubble at the nozzle exit due to flow separation.

5. Conclusions

This study investigates the passive control of base pressure at supersonic Mach number $M = 1.7$ for an area ratio of 4 using quarter ribs, analyzing the effects of rib size, rib location, nozzle pressure ratio (NPR), and rib orientation. The findings demonstrate that the introduction of ribs significantly influences shear layer interactions, leading to variations in base pressure depending on rib size, placement, and orientation. The rib with a 1.5 mm radius increases base pressure by 50%, equivalent to the back pressure. Additionally, a 3 mm rib increases base pressure by 240%, making it ideal for applications that require a base pressure higher than the ambient pressure. Subsequently, passive control proves highly effective in reducing suction within the recirculation zone when a 3 mm rib is positioned at $L/D = 2$ or 3.0.

Furthermore, rib location also plays a crucial role in influencing base pressure recovery. There is a mixed trend for rib radius 1.5 mm when placed at different locations. The rib size cannot decrease the base suction in the recirculation zone. However, the small rib radius has increased the base pressure ratio from 0.4 to 0.8, and the base pressure ratio for the rib radius of 3 mm is from 1.2 to 2.4.

The study further establishes that variations in duct length do not introduce significant changes in base pressure trends, reaffirming that the primary factors governing flow behavior are the rib's geometric properties and its interaction with the shear layer. However, at $L = 0.5\mathrm{D},$ flow oscillations are observed due to its proximity to the nozzle exit, where the shear layer remains in a transitional state before stable reattachment occurs. Ultimately, these results serve as a technological demonstration, highlighting the importance of selecting an appropriate combination of parameters to meet specific mission requirements.

Future studies can focus on enhancing accuracy by implementing advanced turbulence models to more accurately predict flow separation and vortex dynamics. Moreover, exploring hybrid control strategies that combine passive methods with active techniques, such as micro-jets or plasma actuators, could further enhance pressure recovery and reduce drag, leading to more efficient aerodynamic systems. Machine learning techniques can be integrated to optimize rib configurations and predict base pressure variations under different conditions.

References

[1] A. Khan, P. Rajendran, J. S. S. Sidhu and M. Sharifpur, Experimental investigation of suddenly expanded flow at sonic and supersonic Mach numbers using semi-circular ribs: a comparative study between experimental, single layer, deep neural network (SLNN and DNN) models, European Physical Journal Plus 138(4) (2023), 314. https://doi.org/10.1140/epjp/s13360-023-03853-1.

[2] A. Khan, N. M. Mazlan and E. Sulaeman, Effect of ribs as passive control on base pressure at sonic Mach numbers, CFD Letters 14(1) (2022), 140-151. https://doi.org/10.37934/cfdl.14.1.140151.

[3] A. Khan, S. A. Khan, V. Raja, A. Aabid and M. Baig, Effect of ribs in a suddenly expanded flow at sonic Mach number, Heliyon 10(9) (2024), e30313. https://doi.org/10.1016/j.heliyon.2024.e30313.

[4] A. Khan, N. M. Mazlan and M. A. Ismail, Numerical simulation of suddenly expanded flow from converging nozzle at sonic Mach number, Lecture Notes in Mechanical Engineering, 2020, pp. 349-359. https://doi.org/10.1007/978-981-15-4756-0_29.

[5] A. Khan, M. N. Akhtar, A. Aabid, M. Baig and S. A. Khan, Comprehensive CFD analysis of base pressure control using quarter ribs in sudden expansion duct at sonic Mach numbers, International Journal of Thermofluids 24 (2024), 100908. https://doi.org/10.1016/j.ijft.2024.100908.

[6] A. Khan, M. N. Akhtar, S. A. Khan, A. Aabid and M. Baig, Base pressure control with semi-circular ribs at critical Mach number, Fluid Dynamics and Materials Processing 20(9) (2024), 2007-2028. https://doi.org/10.32604/fdmp.2024.049368.

[7] T. Nurhanis, S. A. Khan, A. Khan and M. N. Akhtar, Control of base pressure at supersonic Mach number in a suddenly expanded flow, Journal of Advanced Research in Fluid Mechanics and Thermal Sciences 109(1) (2023), 210-225. https://doi.org/10.37934/arfmts.109.1.210225.

[8] A. A. Ahmad Fakhruddin, S. A. Khan, F. A. Ghasi Mahboobali, M. N. Akhtar and K. A. Pathan, Analysis of base pressure control with ribs at Mach 1.2 using CFD method, Journal of Advanced Research in Fluid Mechanics and Thermal Sciences 123(1) (2024), 108-143. https://doi.org/10.37934/arfmts.123.1.108143.

[9] A. Khan, N. M. Mazlan and M. A. Ismail, Velocity distribution and base pressure analysis of under-expanded nozzle flow at Mach 1.0, Journal of Advanced Research in Fluid Mechanics and Thermal Sciences 92(1) (2022), 177-189. https://doi.org/10.37934/arfmts.92.1.177189.

[10] F. A. Khan, A. A. Ibrahim, M. S. Rais, A. Khan and M. N. Akhtar, Performance analysis of supervised learning algorithms based on classification approach, 2019 6th IEEE International Conference on Engineering Technologies and Applied Sciences (ICETAS), IEEE, 2019. DOI: 10.1109/ICETAS48360.2019.9117394.

[11] A. Mishra, A. Khan and N. Musfirah Mazlan, Determination of shock standoff distance for wedge at supersonic flow, International Journal of Engineering Transactions A: Basics 32(7) (2019), 1049-1056. DOI: 10.5829/ije.2019.32.07a.19.

[12] Z. I. Chaudhary, A. Khan, S. A. Khan and K. A. Pathan, Base pressure control using quarter-circle rib in a suddenly expanded duct at screech prone Mach number $M = 1.8$, CFD Letters 17(8) (2025), 60-95. https://doi.org/10.37934/cfdl.17.8.6095.

[13] F. A. G. Mahaboobali, A. Khan, M. N. Akhtar, S. A. Khan and K. A. Pathan, Passive control of base flows and impact of quarter rib radius and locations at sonic Mach number, Journal of Advanced Research in Numerical Heat Transfer 30(1) (2025), 47-81. https://doi.org/10.37934/arnht.30.1.4781.

[14] Z. I. Chaudhary, A. Khan, S. A. Khan, M. N. Akhtar and K. A. Pathan, Control of suddenly expanded flow using quarter rib for area ratio 4.84 at Mach 2, Journal of Advanced Research in Experimental Fluid Mechanics and Heat Transfer 19(1) (2025), 1-29. https://doi.org/10.37934/arfmts.19.1.129.

[15] A. Khan, M. N. Akhtar, A. Aabid, M. Baig and S. A. Khan, Supersonic flow control with quarter rib in a duct: an extensive CFD study, International Journal of Thermofluids 26 (2025), 101060. https://doi.org/10.1016/j.ijft.2025.101060.

[16] S. Shetty, F. A. G. Mahaboobali, A. Khan, S. A. Khan and K. A. Pathan, Base pressure control using quarter rib at Mach 1.3: a comprehensive CFD analysis, Journal of Advanced Research in Fluid Mechanics and Thermal Sciences 127(2) (2025), 1-32. https://doi.org/10.37934/arfmts.127.2.132.

[17] S. A. I. Bellary, A. Khan, M. N. Akhtar, S. A. Khan and K. A. Pathan, Numerical simulations of base pressure and its control in a suddenly expanded duct at Mach 1.6 using quarter circular ribs, Journal of Advanced Research in Fluid Mechanics and Thermal Sciences 127(2) (2025), 203-233. https://doi.org/10.37934/arfmts.127.2.203233.

[18] S. A. I. Bellary, S. A. Dabir, J. H. Shaikh, T. Tamhane and A. Khan, Computational analysis of thrust generated by converging-diverging nozzle at different diverging angle, Journal of Advanced Research in Numerical Heat Transfer 29(1) (2025), 102-128. https://doi.org/10.37934/arnht.29.1.102128.

[19] F. N. D. M. Anuar, S. A. Khan, F. A. G. Mahaboobali, A. Khan and M. N. Akhtar, Effect of cavity geometry and location on base pressure in a suddenly expanded flow at Mach 2.0 for area ratio 3.24, Journal of Advanced Research in Applied Mechanics 117(1) (2024), 1-21. https://doi.org/10.37934/aram.117.1.121.

[20] M. Bashir, P. Rajendran, A. Khan, V. Raja and S. A. Khan, Numerical investigation of turbulence models with emphasis on turbulent intensity at low Reynolds number flows, Advances in Aircraft and Spacecraft Science 10(4) (2023), 303-315. https://doi.org/10.12989/aas.2023.10.4.303.

[21] M. A. A. Baig, S. A. Khan, F. Al-Mufadi and E. Rathakrishnan, Control of base flows with microjets, International Journal of Turbo and Jet Engines 28(1) (2011), 59-69. DOI: 10.1515/tjj.2011.009.

[22] S. Rehman and S. A. Khan, Control of base pressure with micro-jets: Part I, Aircraft Engineering and Aerospace Technology 80(2) (2008), 158-164. https://doi.org/10.1108/00022660810859373.

[23] M. Faheem, S. Afghan Khan, W. Asrar, A. Khan and R. Kumar, Experimental study on the mean flow characteristics of a supersonic multiple jet configuration, Aerospace Science and Technology 108 (2021), 106377. DOI: 10.1016/j.ast.2020.106377.

[24] M. F. M. Sajali, A. Aabid, S. A. Khan, E. Sulaeman and F. A. G. Mehaboobali, Numerical investigation of the flow field of a non-circular cylinder, CFD Letters 11(5) (2019), 37-49. https://www.akademiabaru.com/submit/index.php/cfdl/article/view/3161.

[25] S. A. Khan, M. Asadullah, G. M. Fharukh Ahmed, A. Jalaluddeen and M. A. Ali Baig, Passive control of base drag in compressible subsonic flow using multiple cavities, International Journal of Mechanical and Production Engineering Research and Development 8(4) (2018), 39-44. DOI: 10.24247/ijmperdaug20185.

[26] S. A. Khan, M. A. Fatepurwala, K. N. Pathan, P. S. Dabeer and M. A. A. Baig, CFD analysis of human-powered submarine to minimize drag, International Journal of Mechanical and Production Engineering Research and Development 8(3) (2018), 1057-1066. DOI: 10.24247/ijmperdjun2018111.

[27] S. A. Khan, Mohammed Asadullah and Jafar Sadiq, Passive control of base drag employing dimple in subsonic suddenly expanded flow, International Journal of Mechanical and Mechatronics Engineering IJMME-IJENS 18(3) (2018), 69-74.

[28] A. Aabid, M. Baig, M. A. Murtuza and S. A. Khan, Optimization of dry sliding wear behavior of aluminium-based hybrid MMC’s using experimental and DOE methods, Journal of Materials Research and Technology 16 (2022), 743-763. https://doi.org/10.1016/j.jmrt.2021.12.005.

[29] E. Rathakrishnan, Effect of ribs on suddenly expanded flows, AIAA Journal 39(7) (2001), 1402-1404. https://doi.org/10.2514/2.1461.